# TECHNICAL MEMORANDUM

## X-240

# HYPERSONIC LONGITUDINAL TRIM, STABILITY, AND CONTROL CHARACTERISTICS OF A DELTA-WING CONFIGURATION AT HIGH ANGLES OF ATTACK

By William H. Close

Langley Research Center
Langley Field, Va.



NATIONAL AERONAUTICS AND SPACE ADMINISTRATION

WASHINGTON

April 1960

[redacted]

NATIONAL AERONAUTICS AND SPACE ADMINISTRATION

TECHNICAL MEMORANDUM X-240

# HYPERSONIC LONGITUDINAL TRIM, STABILITY, AND CONTROL CHARACTERISTICS OF A DELTA-WING CONFIGURATION AT HIGH ANGLES OF ATTACK*

By William H. Close

## SUMMARY



An investigation has been made in the Langley 11-inch hypersonic tunnel to determine the ability to trim and maintain static longitudinal stability and control of a delta-wing configuration at high angles of attack. Three-component force tests were made at a Mach number of 6.7 and a Reynolds number of $0.47 \times 10^6$ (based on root chord) at angles of attack from $27^\circ$ to $56^\circ$. It was found that the wings with the center of gravity located at 42 percent of the mean aerodynamic chord could be trimmed throughout the test angle-of-attack range without loss in longitudinal stability and control. If the center of gravity can be located farther rearward, the sometimes large losses in lift due to trimming can be avoided (as less control would then be required in order to trim) without necessarily decreasing stability. Positive nose deflections yielded small pitching-moment increments at the higher angles of attack, but were stabilizing throughout the test angle-of-attack range. Negative flap deflections produced large pitching-moment increments and were destabilizing for all angles of attack. Unported trailing-edge flaps were found to be generally less effective than the smooth-bottom flaps.

A method of predicting the longitudinal characteristics is presented with typical results which show good agreement with measured data for the flat wing and wing-flap deflections. Interference effects due to the nose deflection were not predicted, however, and the predictions for nose deflections were generally not as good as those for flap deflections.

*Title, Unclassified.

## INTRODUCTION

Some recent studies concerning the problems of reentry (such as refs. 1 and 2) have shown the desirability of winged configurations capable of generating high lift or high drag or both. Tests at a Mach number of 6.8 have indicated that lift coefficients of 0.7 to 0.8 should be obtainable for untrimmed wings at an angle of attack of approximately 50°. Little (if any) data are available, however, on the ability to trim, stabilize, and control wings at such high lift coefficients and angles of attack. Therefore an investigation was undertaken in the Langley 11-inch hypersonic tunnel at a Mach number of 6.7 and a Reynolds number of $0.47 \times 10^6$ (based on root chord) to determine the ability to trim and control a 70° swept delta wing at high angles of attack (27° to 56°) through the use of deflectable-nose and trailing-edge-flap panels. Consideration was also given to the problem of minimizing lift losses due to trimming.

## SYMBOLS

Lift, drag, and pitching moment were referred to the wind-axis system and normal force was referred normal to the wing center panel as shown in figure 1. Unless otherwise stated, the pitching moment was referred to a center-of-gravity location at 42 percent of the mean aerodynamic chord which is approximately the subsonic aerodynamic-center location. (See ref. 3.)

$C_D$ drag coefficient, Drag/qS

$C_L$ lift coefficient, Lift/qS

$C_N$ normal-force coefficient, Normal force/qS

$C_{N,SD}$ normal-force coefficient at shock detachment

$C_{N_o}'$ "maximum normal-force coefficient," $\frac{2}{\gamma \beta M_\infty}\left(\frac{p_{t_2}}{p_1}\right)_{M_N}$

$C_{N_\alpha}$ slope of normal-force coefficient with angle of attack, $\frac{\partial C_N}{\partial \alpha}$, per deg

$C_{m_\alpha}$ stability level, $\frac{\partial C_m}{\partial \alpha}$, per deg

$C_m$ pitching-moment coefficient, $\frac{\text{Pitching moment}}{qS\bar{c}}$

$-\frac{\partial C_m}{\partial C_N}$ static margin

$\Delta C_m$ incremental pitching moment produced by a control deflection or control-area change

$C_{m_\delta}$ control effectiveness derivative at zero deflection, $\left(\frac{\partial \Delta C_m}{\partial \delta}\right)_{\delta=0}$, per deg

$\frac{\partial \Delta C_{m,n}}{\partial (S_n/S)}$ nose-control-area effectiveness derivative at zero area

$\frac{\partial \Delta C_{m,f}}{\partial (S_f/S)}$ flap-control-area effectiveness derivative at zero area

$c$ wing root chord, in.

$\bar{c}$ wing mean aerodynamic chord, 3.00 in.

$M_\infty$ free-stream Mach number

$M_N$ Mach number normal to the wing leading edge in the plane formed by wing leading edge and free-stream velocity vector

$\left(\frac{p_{t_2}}{p_1}\right)_{M_N}$ ratio of stagnation pressure behind normal shock to static pressure ahead of shock as determined by Mach number normal to leading edge, $\left[\frac{(\gamma+1)M_N^2}{2}\right]^{\frac{\gamma}{\gamma-1}}\left[\frac{\gamma+1}{2\gamma M_N^2-(\gamma-1)}\right]^{\frac{1}{\gamma-1}}$

$q$ free-stream dynamic pressure, lb/sq in.

$S$ wing plan-form area, 7.378 sq in.

$S_f$ flap plan-form area, sq in.

$S_n$ nose plan-form area, sq in.

$t$ maximum thickness, in.

$\alpha$ angle of attack referenced to center wing panel, deg

$\beta$ $\sqrt{M_\infty^2 - 1}$

$\gamma$ ratio of specific heats, 1.4 for air

$\delta$ control deflection angle, deg

$\epsilon$ semiapex angle of wing, deg

$\theta_\delta$ total flow deflection angle normal to leading edge, $\theta_{fp} + \theta_t$, deg

$\theta_{fp}$ flat-plate flow deflection angle normal to the leading edge, deg

$\theta_t$ flow deflection angle normal to the leading edge, due to thickness ($0^\circ$ for flat-plate wings), deg

$\theta_{SD}$ total flow deflection angle normal to the leading edge for shock detachment, deg

$\chi'$ normal-force correlation parameter, $\dfrac{\sin^2\theta_{fp} - \sin^2(\theta_{SD} - \theta_t)}{1 - \sin^2(\theta_{SD} - \theta_t)}$

$\xi$ normal-force parameter, $\dfrac{C_N - C_{N_{SD}}}{C_{N_o}' - C_{N_{SD}}}$

Subscripts:

c center panel

f flap panel

fp flat-plate wing

n nose panel

SD shock detachment

t trim or thickness

## MODELS AND TESTS

The basic dimensions of the models tested are presented in figure 2. The delta wing was swept 70° at the leading edge and had a small leading-edge radius. By using a 30° adapter, tests were made with wings 1, 2, 3, and 4 through angles of attack from 27° to 56° (corresponding to balance angles of attack from -3° to 26°). Nose and flap deflections were set by bending along the grooves milled across the top of the wing as shown in figure 2(a). The base pressure of the adapter was measured and set equal to free-stream pressure, but other aerodynamic forces on the adapter were negligible. Several runs were made with wing 5 and a 0° adapter (shown in fig. 2(b)) to obtain low-angle-of-attack stability characteristics of the undeflected wing. The effects of this adapter were calculated by modified Newtonian theory and were subtracted from the measured data.

Another wing was constructed with the same dimensions as wing 3 but with the flap made separately and mounted to the wing by a set of fixed-angle rigid supports on top of the wing. Through the use of various supports the flap deflection angles could be varied as well as the effective hinge line. With this model (designated wing U) a study was made of the effects of unported flaps. With the flaps hinged rearward, the nose of the flap protrudes into the high-pressure stream below the wing, scoops up some of this high-energy flow, and diverts it over the top of the flap to replace the near vacuum which would be present on the smooth-bottom configurations (wings 1 to 4). In order to discern between the two different hinge-line locations, the following model designations were established: U-C represents the configuration with the flap hinge line near the center of the flap chord, U-R represents the configuration with the flap hinge line near the trailing edge of the flap as shown in figure 2(c). A modification to the wing trailing edge was made (as shown also in fig. 2(c)) to open the gap farther between the wing and flap; these configurations were designated U-Cm and U-Rm. Tests were made using the 30° adapter as previously described for wings 1 to 4.

The wings were mounted on a three-component external strain-gage balance in the Mach number 6.86, Invar nozzle of the Langley 11-inch hypersonic tunnel. In this nozzle the test-section Mach number varies slightly with stagnation pressure, and with the stagnation pressure set for these tests at 118 pounds per square inch absolute, the free-stream Mach number was 6.7 and the Reynolds number was $0.47 \times 10^6$ based on root chord. An average running time of 90 seconds allowed the full range of angle of attack (27° to 56°) to be obtained on most runs. The Mach number variations during the runs were less than 0.06. Variations in $q$ were accounted for in the data. Stagnation temperatures were kept

above 600° F to avoid liquefaction. (See ref. 4.) Reference 5 presents a more complete description of this facility and of a nozzle similar to the one used for these tests.

## PRECISION OF DATA

The root-mean-square probable errors in the force and moment coefficients for individual test points as a result of measuring inaccuracies and environmental variations are as follows:

| | |
|---|---|
| $dC_L$ | ±0.0150 |
| $dC_D$ | ±0.0089 |
| $dC_m$ | ±0.0065 |

The angles of attack $\alpha$ and the panel deflection angles were accurate to within ±0.10°.

## RESULTS AND DISCUSSION

### Measured Basic Data

The variations in lift, drag, and pitching-moment coefficients with angle of attack are presented in figures 3 to 6 to show the effects of variable control geometry.

The effects of various flap deflections in conjunction with fixed nose deflections are shown in figure 3. An increase in negative flap deflection decreases lift and drag throughout the measured angle-of-attack range. Large, positive pitching-moment increments are produced with negative flap deflection, but the stability level $\left(C_{m_\alpha}\right)$ is reduced, and neutral stability is approached and reached in some cases of large flap deflection. Comparison of figures 3(b) and 3(d) shows the expected increases in increments produced by flap deflection with increased flap area.

Figure 4 shows that increasing positive nose deflection consistently yields decreased lift and increased drag with positive pitching-moment increments that decrease markedly with increasing angle of attack. It should be noted that the pitching-moment coefficient of the configurations with 20° nose deflection repeatedly diminishes to values very close to those obtained for the configurations with 10° nose deflection at angles of attack near 56°. While not contributing large pitching-moment increments at the highest angles of attack, increased nose

deflection does add substantially to the stability level of the configuration because the nose is operating in a region where $C_{N_\alpha}$ is lower than that for the rest of the wing. Therefore it may be anticipated that positive nose deflections will be stabilizing from an angle of attack of approximately 30° (where $C_{N_\alpha}$ is greatest) to 90° and destabilizing at lower angles of attack. The loss in lift associated with increasing nose deflection is most probably a result of nose-flow influence on the rest of the wing at the lower angles of attack. At the higher angles of attack the tilt of the normal-force vector of the nose combines with the nose-flow influence to create the loss in lift.

The effect of variable flap area on the longitudinal stability characteristics of a wing with fixed nose geometry and fixed flap deflections is presented in figure 5. Consistent lift and drag decrements are produced as a nearly linear function of the increase in flap area. Pitching-moment increments do not follow the same trend, as the center of pressure of the flaps moves closer to the center of gravity with increased flap area, thus decreasing the moment arm. The rate of increase of the product of flap area times flap moment arm diminishes as the product approaches its maximum value at $S_f/S = 0.624$ (hinge line at center-of-gravity location). Thus large pitch increments are produced for flap areas of 0.19S and 0.36S, with the flap having an area of 0.51S only slightly more effective than the flap having an area of 0.36S, but still producing additional large decrements in lift and drag.

Figure 6 presents the effects of variable nose area on the longitudinal stability characteristics of the wing with a fixed 10° nose deflection. It can be seen from this figure that increasing the nose area results in a loss of lift at the higher angles of attacks and an increase in drag. Pitching-moment increments resulting from increased nose areas tend to diminish with increasing angle of attack. Increases in stability level $\left(C_{m_\alpha}\right)$ are realized through increased nose area; that is, as nose area increases, more area ahead of the center of gravity is subjected to the aforementioned lower $C_{N_\alpha}$.

## Predictions of Basic Characteristics

Predictions of the longitudinal stability characteristics of the present configuration with various control deflections were made by the method presented in the appendix. These predictions are compared with measured data in figures 7 and 8.

Figure 7 indicates that the predicted coefficients for various flap deflections are in good agreement with the measured values. The shift

in angle of attack for maximum lift, the increase in drag decrement with increased angle of attack, and the increase in pitching-moment increment with increase in angle of attack have been predicted. Closer examination shows that the increments in pitching-moment coefficients are not predicted as accurately as are the increments in lift and drag, undoubtedly as a result of the assumed centers of pressure of the flap being slightly in error. Not predicted, however, are the peculiar shifts in the pitching-moment coefficients between angles of attack of $45^\circ$ and $50^\circ$ which appear throughout the present data. It is believed that this shift is caused by the local flow under the wing changing from supersonic to subsonic between angles of attack of $45^\circ$ and $50^\circ$. The schlieren photographs presented in figure 9(a) seem to verify this assumption by the absence of the strong shock from the flap above $\alpha = 45^\circ$. Schlieren photographs of the smooth-bottom configuration are presented in figure 9(b) for comparison.

Figure 8 presents the comparison of measured and predicted longitudinal stability characteristics with various nose deflections. The computed effects of nose deflection were not in as good agreement with the measured values as were the effects of flap deflections in figure 7. This was probably due to the inability of the present isolated-panel method to predict interference effects produced by the nose on the rest of the wing. The trends illustrated by the measurements were predicted; for example, the crossover of the lift curves and the shift in angle of attack for maximum lift. The predicted pitching-moment curves show the increase in stability (for $\delta_n = 20^\circ$) provided by the deflected nose and also indicate the decrease in nose effectiveness with increased angle of attack.

## Trim

Figures 3 to 6 show that many combinations of control areas and deflections will provide the necessary pitching-moment increments to trim throughout the angle-of-attack range. Figure 10 presents a summary of the combinations tested that did trim within the test angle-of-attack range. These values of trimmed lift coefficient and of static margin at trim are compared with lift-coefficient and static-margin curves for the untrimmed undeflected wing. Increased penalties in lift due to trimming are apparent at the higher angles of attack. The maximum measured trimmed lift coefficient is 0.592 at $\alpha = 48^\circ$ which is 17 percent less than the lift coefficient of 0.715 for the undeflected wing at the same angle of attack. The aforementioned effects of nose and flap deflection on stability are clearly illustrated by the comparison of trimmed static margins. The two points representing trimmed configurations with no nose deflection display lower static margins than those for the undeflected wing while the other points for wings with

positive nose deflection have greater static margins. It is therefore evident that for these cases the stabilizing effect of positive nose deflection more than overcomes the destabilizing tendency of negative flap deflections.

As illustrated in figure 10, the loss of lift due to trimming is substantial. If the center of gravity could be located farther rearward on the vehicle, less control would be required to trim and, consequently, less lift would be lost due to trimming. Rearward locations of the center of gravity would compromise the subsonic characteristics of this configuration (at subsonic speeds this configuration would be expected to be neutrally stable with the center of gravity at $0.42\bar{c}$, see ref. 3), but to illustrate the advantages at hypersonic speeds of such locations, a typical example of the effects of center-of-gravity location on the longitudinal stability characteristics is presented in figure 11.

This figure presents an example of the various configurations that can be trimmed at $\alpha = 52^{\circ}$ (the approximate angle of attack for maximum lift) with various center-of-gravity locations. All points are for trimmed conditions. Open symbols represent experimental data and solid symbols represent data obtained from cross plots at $\alpha = 52^{\circ}$. The trimmed lift coefficients were increased about 0.01 for each percent rearward placement of the center of gravity. Thus from 6 to 10 percent of flat-wing lift can be regained at trim if the center of gravity could be located 6 percent rearward and appropriate flap deflection provided from trim (with fixed nose deflection). It is conceivable that, for angles of attack less than $52^{\circ}$, with positive nose deflection and positive flap deflection all the undeflected-wing lift could be produced or exceeded at trim. Also, as can be seen on the upper portion of this figure, the rearward locations of the centers of gravity do not necessarily decrease the static margin at trim; in fact, for the configuration with $20^{\circ}$ nose deflection, the static margin was increased with more rearward center-of-gravity locations (from $0.43\bar{c}$ to $0.46\bar{c}$). Approximately one percent static margin is lost by deflecting the flap from $-30^{\circ}$ to $-20^{\circ}$ for the configuration with $0^{\circ}$ nose deflection.

## Control and Control-Area Parameters

The control effectiveness derivatives are presented in figure 12 and are compared with the predictions calculated by the method presented in the appendix. As can be seen in this figure, the nose effectiveness generally decreases slightly with increased angle of attack as a result of reduced $C_{N_\alpha}$ of the nose. The nose effectiveness derivatives are influenced only slightly by flap deflection as displayed by the small differences between the three nose-effectiveness curves for configurations with different flap deflections. The prediction is shown as a

single line since the isolated-panel concept which was used for the predictions cannot account for interactions of the various panels. The flap effectiveness derivatives are substantially affected by the nose geometry. With a fixed nose deflection of 0° the flap effectiveness remains almost constant with angle of attack; however, as the nose deflection is increased, the flap effectiveness at the lower angles of attack is reduced. Unpublished results from an investigation at Mach number 5 of a configuration having a flat-bottom wing with deflected nose indicated that vortices were generated at the intersection of the wing leading edge and nose-panel hinge line. These vortices increased in width with downstream distance along the wing. Some evidence of the altered flow pattern at $M_\infty = 9.6$ is indicated by figure 13. It may be seen that nose deflection produced inward deviations of flow direction, which may be the result of the aforementioned vorticity. It is believed that this flow deviation was the predominant cause of the reduced magnitude of $C_{m_{\delta_f}}$ and the large variations in $C_{m_{\delta_f}}$ with $\alpha$ in the lower angle-of-attack range (fig. 12). The predicted values for the flap effectiveness did not agree with the experimental values as well as did the prediction for the nose, largely because of the inability to predict the center of pressure of the flap and the flow deviation. Flap centers of pressure found experimentally were located quite far rearward of the center of area and in some cases were located behind the flap trailing edge.

The control-area effectiveness derivatives

$$\frac{\partial \Delta C_{m_n}}{\partial (S_n/S)} \quad \text{and} \quad \frac{\partial \Delta C_{m_f}}{\partial (S_f/S)}$$

are presented in figure 14. These parameters are the slopes, at zero control-surface area, of the curves for the incremental pitching moment produced by control deflection plotted against the control-surface area ratio. These values can be used as reasonable guides in the selection of feasible control areas. It can be seen from this figure that the nose-area effectiveness decreases markedly up to about 40° angle of attack and thereafter remains nearly constant at a quite low value of 0.1. The flap-area effectiveness parameters, on the other hand, display consistent increases with increasing angle of attack. Predicted values obtained by the method presented in the appendix are in fair agreement with the experimental data.

## Unported Flaps

In an effort to increase flap effectiveness, wing U was designed so that the flaps would be hinged rearward and the leading edge of the

flap could protrude down (unport) into the high-pressure flow beneath the wing, thus deflecting high-pressure flow over the top of the flap and maintaining low pressure on the bottom surface of the flap.

The effects of variable flap deflection for wings U-R, U-C, U-Rm, and U-Cm are presented in figures 15(a), 15(b), 15(c), and 15(d), respectively. The data presented herein repeatedly display decreased lift and drag together with positive pitching-moment increments when the flaps are set at negative deflection angles. Generally greater losses in lift and smaller reductions in drag resulted from the rear-hinged flaps (wings U-R and U-Rm, see figs. 15(a) and 15(c)) as compared to the center-hinged flaps (wings U-C and U-Cm, see figs. 15(b) and 15(d)) or the front-hinged, smooth-bottom flaps (wing 3, see fig. 3(d)). The wing modification (which was intended to open the gap farther between the wing and flap in order that more high-pressure air could be deflected over the top of the flap) generally resulted in slight reductions in lift and drag.

Figure 16 compares the flap effectiveness derivatives of the unported-flap configurations and the comparable smooth-bottom configuration (wing 3). Below $50^\circ$ angle of attack the flaps of the smooth-bottom configuration have the highest effectiveness and the center-hinged unported flaps have greater effectiveness than the rear-hinged unported flaps. The lower effectiveness of the unported flaps may well be caused by the relatively thick boundary layer below the wing, the flap-support-system interference, and the losses through the strong shock on the leading edge of the flap. The support struts protruded farther ahead of the flap leading edge on the rear-hinged flaps than on the center-hinged flaps and this difference in strut location relative to the flaps is probably the cause of the further reduction of effectiveness for the rear-hinged flaps. The carbon-black and oil streak photographs presented in figure 17 give vivid illustration of the complicated flow field on the unported flaps. (See also schlieren photographs of figure 9(a).) Note particularly the shock-induced separation region on the modified wing trailing edge. Although the present unported flaps did not produce the increased effectiveness hoped for at the onset of this investigation, variations of this scheme may in the future prove to be more efficient.

## CONCLUSIONS

An investigation has been made in the Langley 11-inch hypersonic tunnel at a Mach number of 6.7 and a Reynolds number of $0.47 \times 10^6$ based on root chord to determine the ability to trim and maintain static longitudinal stability and control of a $70^\circ$ swept delta wing

at high angles of attack (from 27° to 56°). The results of this investigation have led to the following conclusions:

1. The present delta-wing configuration with the center of gravity located at 42 percent of the mean aerodynamic chord (center-of-gravity location for subsonic neutral stability) can be trimmed and controlled throughout the test angle-of-attack range through the use of deflected-nose and trailing-edge-flap panels, generally without loss in longitudinal stability.

2. With the center of gravity located at 42 percent of the mean aerodynamic chord, the loss in lift due to trimming was as great as 17 percent at an angle of attack of 48°; however, if the center of gravity can be located farther rearward this loss in lift can be reduced to near zero (because of the reduced control required to trim) with no loss in stability.

3. Nose-panel control effectiveness decreased with increased angle of attack, but positive nose deflection yielded increased stability throughout the test angle-of-attack range. Conversely, the flap-control effectiveness increased with angle of attack and negative flap deflections were destabilizing.

4. The use of unported flaps in an attempt to increase flap effectiveness above that for the smooth-bottom configuration was generally unsuccessful probably because of the relatively thick boundary layer and losses through the shock waves generated by the blunted flap leading edge and supports.

5. A method is presented that predicts the longitudinal characteristics of the present configurations with good accuracy for the undeflected wing and the wing with flap deflections, but predictions for the wing with nose deflections are not as good because of the inability of this method to cope with the apparent interference effects produced by the nose.

Langley Research Center,
National Aeronautics and Space Administration,
Langley Field, Va., November 13, 1959.

## APPENDIX

## SEMI-EMPIRICAL METHOD OF PREDICTION

The semi-empirical predictions presented herein were obtained from a modification of a method presented in reference 7. The present method utilizes two-dimensional oblique-shock pressure predictions for the lower surface and two-dimensional Prandtl-Meyer expansion pressure predictions for the upper surface when the oblique shock is attached to the leading edge (leading-edge bluntness ignored). Above shock detachment an empirical normal-force correlation curve similar to that presented in reference 7 is used which relates the normal-force coefficient to a "maximum normal-force coefficient" $\left(C_{N_o}'\right)$.

The following procedure is used to predict the normal force of the deflected wing above shock detachment. The first step is to determine the angle of attack for leading-edge shock detachment. This may be accomplished by the methods of reference 6 or by the following graphical method. Compute the Mach number normal to the wing leading edge

$$M_N = M_\infty \sqrt{1 - \cos^2\alpha \cos^2\epsilon}$$

for various angles of attack, and from figure 18 (obtained from ref. 7 or 8) determine the corresponding flow deflection angles for shock detachment, $\theta_{SD}$. Compute the flow deflection angles for the wing under study

$$\theta_\delta = \theta_{fp} + \theta_t = \tan^{-1}\left(\frac{\tan\alpha}{\sin\epsilon}\right) + \tan^{-1}\left(\frac{t/c}{\sin\epsilon}\right)$$

for various angles of attack. The angle of attack for which $\theta_\delta = \theta_{SD}$ (see fig. 18, $\theta_{SD}$ plotted against $M_N$) is the angle of attack for shock detachment $\alpha_{SD}$. If $\theta_{SD}$ is everywhere less than $\theta_\delta$, the assumption must be made that the angle of attack for shock detachment is $0^\circ$. For each angle of attack above $\alpha_{SD}$ evaluate the parameter

$$\chi' = \frac{\sin^2\theta_{fp} - \sin^2(\theta_{SD} - \theta_t)}{1 - \sin^2(\theta_{SD} - \theta_t)}$$

and obtain the corresponding value of

$$\xi = \frac{C_N - C_{N,SD}}{C_{N_o}' - C_{N,SD}}$$

from figure 19 which was derived from unpublished data from the Langley 11-inch tunnel, data from reference 10, and data from the present undeflected wing. (Note in fig. 19 the comparison of measured values for the present wing and values calculated by using modified Newtonian theory.) Therefore

$$C_N = \xi C_{N_o}' + (1 - \xi) C_{N,SD}$$

where $C_{N,SD}$ is the normal-force coefficient as determined by the shock-expansion method at $\alpha_{SD}$ and $C_{N_o}'$ is a "maximum normal-force coefficient" determined as follows for each angle of attack:

$$C_{N_o}' = \frac{2}{\gamma \beta M_\infty} \left( \frac{p_{t_2}}{p_1} \right)_{M_N}$$

where $\beta = \sqrt{M_\infty^2 - 1}$ and $\left( \frac{p_{t_2}}{p_1} \right)_{M_N}$ is the ratio of the stagnation pressure behind a normal shock to the static pressure ahead of the shock as determined by the Mach number normal to the leading edge, or more precisely stated

$$\left( \frac{p_{t_2}}{p_1} \right)_{M_N} = \left[ \frac{(\gamma + 1) M_N^2}{2} \right]^{\frac{\gamma}{\gamma - 1}} \left[ \frac{\gamma + 1}{2\gamma M_N^2 - (\gamma - 1)} \right]^{\frac{1}{\gamma - 1}}$$

(the Rayleigh pitot formula). Tabulation of $\left( \frac{p_{t_2}}{p_1} \right)^{-1}$ may be found in reference 9. Figure 20 shows the excellent agreement between measured normal-force coefficient for the undeflected wing and the values predicted by this method.

Lift is then determined as

$$C_L = C_N \cos \alpha$$

and drag due to lift is

$$C_{D_L} = C_L \tan \alpha = C_N \sin \alpha \approx C_D$$

for the flat wing. For deflected-panel configurations the angle of incidence of each panel to the free stream $(\alpha + \delta)$ is considered the angle of attack for that panel and from figure 20 the normal-force coefficient corresponding to that angle is assumed as the pressure

coefficient of the panel (isolated-panel concept). Therefore the contribution of lift due to the nose panel is

$$C_{L,n} = C_{N(\alpha + \delta_n)} \cos(\alpha + \delta_n) \frac{S_n}{S}$$

and of that due to the flap panel is

$$C_{L,f} = C_{N(\alpha + \delta_f)} \cos(\alpha + \delta_f) \frac{S_f}{S}$$

The lift of the center panel is assumed to follow the relation

$$C_{L,c} = C_{N(\alpha)} \cos(\alpha) \frac{S_c}{S}$$

In the preceding lift relations, the parenthetical subscripts of the normal-force coefficients indicate the values of the angles of attack to which those normal-force coefficients correspond on figure 20. The drag relations could be obtained by replacing the cosines in the preceding lift relations with the sines of the same angles. All drag calculations presented herein are for drag due to lift and do not include skin friction, base drag, or leading-edge pressure drag.

For the flat, undeflected wing the experimental center of pressure was found to be slightly rearward of the $0.51\bar{c}$ position or $0.01\bar{c}$ behind the center of projected area (which is roughly at the center of the lower-surface slab area). Therefore all calculations were made using a center-of-pressure location at $67\frac{1}{3}$ percent of the panel length for triangular panels. Flap centers of pressure were calculated so that the resultant centers of pressure of the undeflected flap and preceding triangular panel would place the overall undeflected configuration center of pressure at $0.51\bar{c}$. The panel pressure coefficients (as determined in the lift calculations) are then applied over the appropriate lever arms to calculate pitching-moment coefficients.

## REFERENCES


1. Grant, Frederick C.: Importance of the Variation of Drag With Lift in Minimization of Satellite Entry Acceleration. NASA TN D-120, 1959.

2. Staff of Langley Flight Research Division (Compiled by Donald C. Cheatham): A Concept of a Manned Satellite Reentry Which Is Completed With a Glide Landing. NASA TM X-226, 1959.

3. Paulson, John W., and Shanks, Robert E.: Investigation of Low-Subsonic Flight Characteristics of a Model of a Flat-Bottom Hypersonic Boost-Glide Configuration Having a 78° Delta Wing. NASA TM X-201, 1959.

4. McLellan, Charles H., and Williams, Thomas W.: Liquefaction of Air in the Langley 11-Inch Hypersonic Tunnel. NACA TN 3302, 1954.

5. McLellan, Charles H., Williams, Thomas W., and Beckwith, Ivan E.: Investigation of the Flow Through a Single-Stage Two-Dimensional Nozzle in the Langley 11-Inch Hypersonic Tunnel. NACA TN 2223, 1950.

6. Bertram, Mitchel H., and McCauley, William D.: Investigation of the Aerodynamic Characteristics at High Supersonic Mach Numbers of a Family of Delta Wings Having Double-Wedge Sections With the Maximum Thickness at 0.18 Chord. NACA RM L54G28, 1954.

7. Post, J.: Lift and Drag-Due-to-Lift of Thin Delta Wings at Hypersonic Speeds and High Angles of Attack. SR-126-TM-A-6, CONVAIR.

8. Burcher, Marie A.: Compressible Flow Tables for Air. NACA TN 1592, 1948.

9. Ames Research Staff: Equations, Tables and Charts for Compressible Flow. NACA Rep. 1135, 1953. (Supersedes NACA TN 1428.)

10. Lampert, Seymour: Aerodynamic Force Characteristics of Delta Wings at Supersonic Speeds. Rep. No. 20-82 (Contract No. DA-04-495-Ord 18), Jet Propulsion Lab., C.I.T., Sept. 9, 1954.

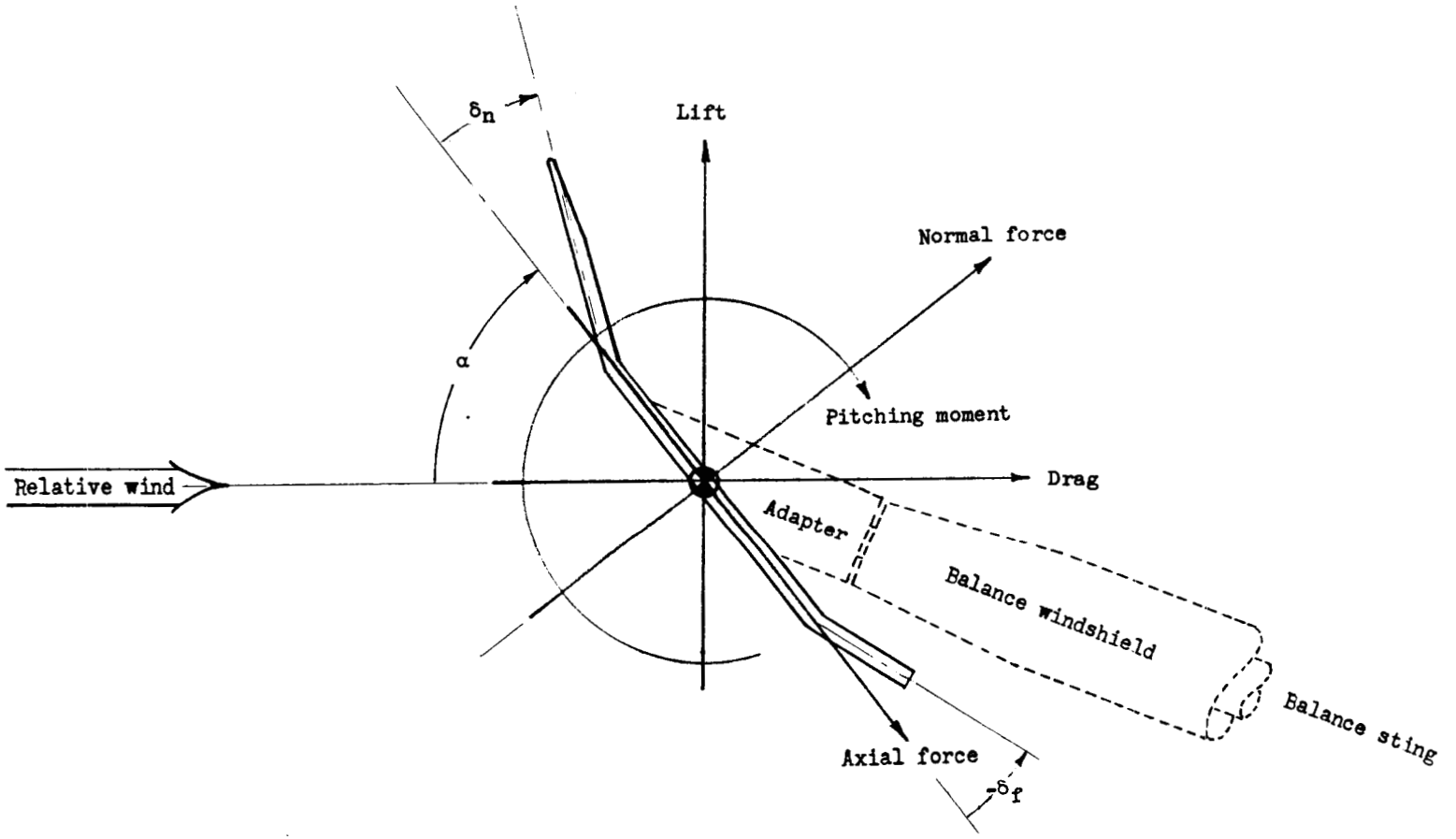


Figure 1.- System of reference axes. Arrows indicate positive directions unless otherwise noted.

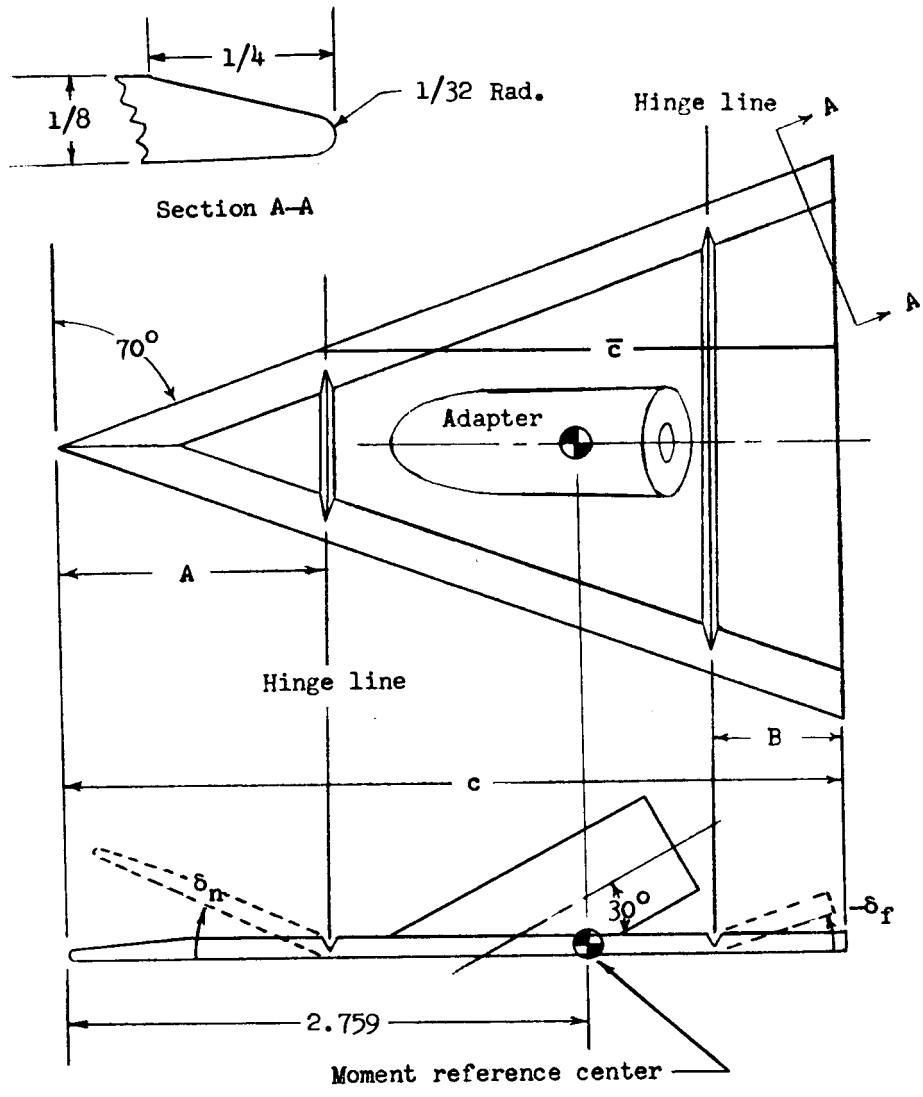


| WING | c | A | B | $S_n/S$ | $S_f/S$ |
|---|---|---|---|---|---|
| 1 | 4.500 | .900 | .450 | .04 | .19 |
| 2 | 4.500 | 1.800 | .450 | .16 | .19 |
| 3 | 4.500 | 1.800 | .900 | .16 | .36 |
| 4 | 4.500 | 1.800 | 1.350 | .16 | .51 |

(a) Wings 1, 2, 3, and 4.

Figure 2.- Model dimensions. All linear dimensions in inches.

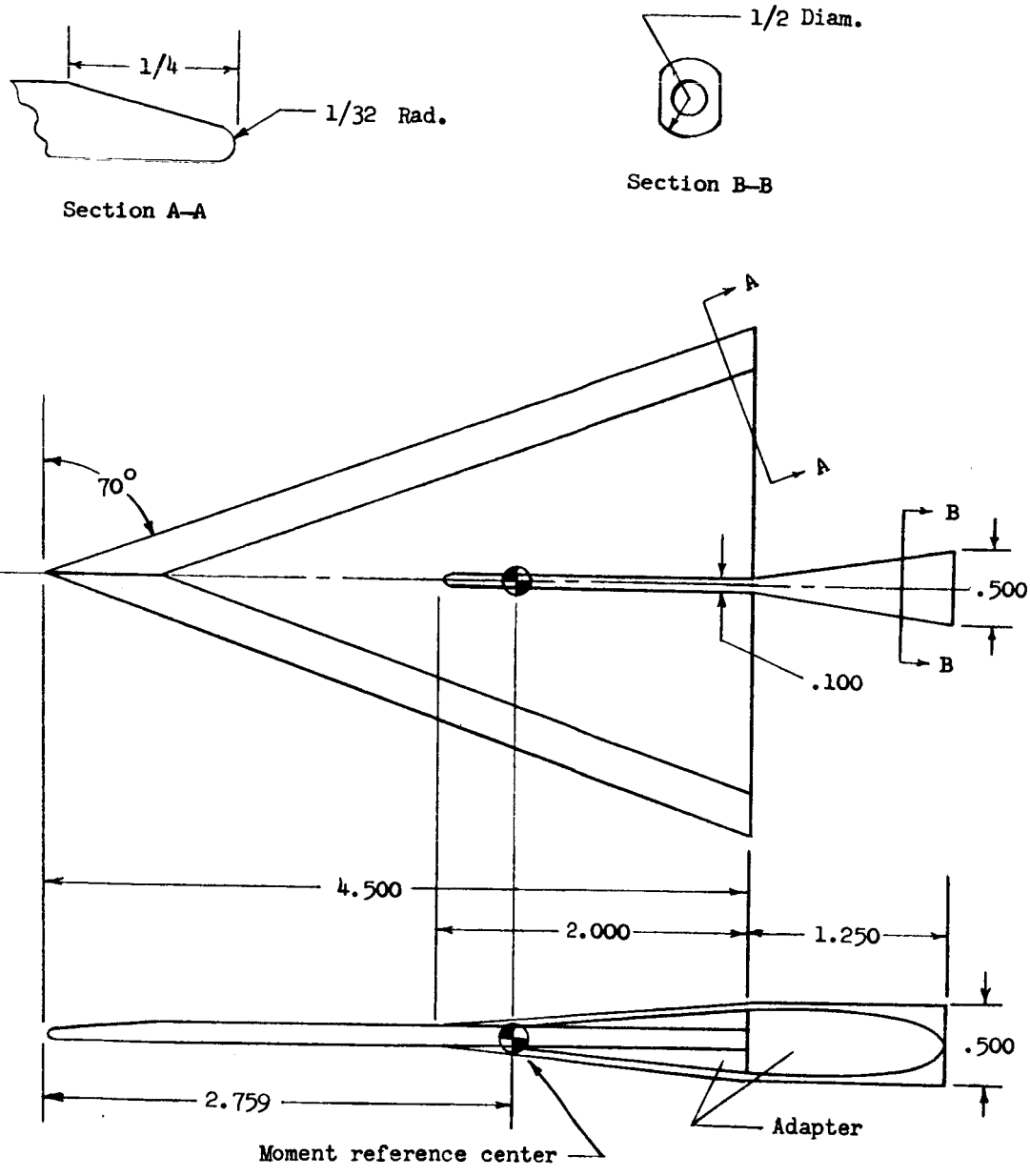


(b) Wing 5.

Figure 2.- Continued.

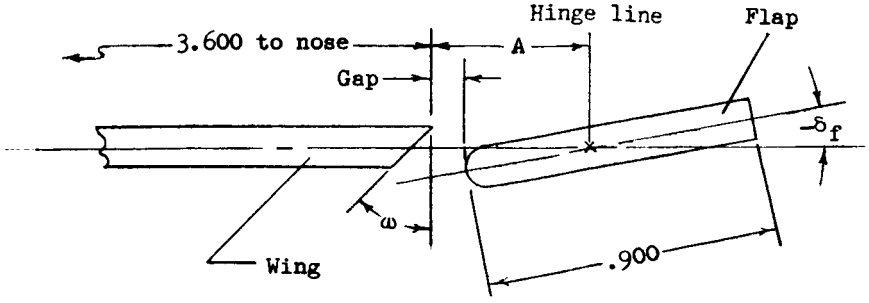


| WING | $\delta_f$ | A | GAP | ω |
|---|---|---|---|---|
| U-C | 0° | .390 | .035 | 0° |
| U-C | -10° | .390 | .035 | 0° |
| U-C | -20° | .390 | .035 | 0° |
| U-Cm | 0° | .390 | .035 | 45° |
| U-Cm | -10° | .390 | .035 | 45° |
| U-Cm | -20° | .390 | .035 | 45° |

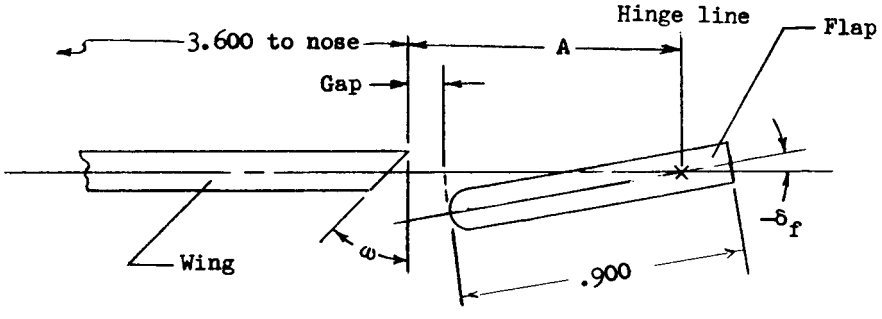


| WING | $\delta_f$ | A | GAP | ω |
|---|---|---|---|---|
| U-R | 0° | .830 | .035 | 0° |
| U-R | -10° | .830 | .035 | 0° |
| U-R | -20° | .830 | .035 | 0° |
| U-Rm | 0° | .830 | .035 | 45° |
| U-Rm | -10° | .830 | .035 | 45° |
| U-Rm | -20° | .830 | .035 | 45° |

(c) Flap and wing-trailing-edge details for wing U.

Figure 2.- Concluded.

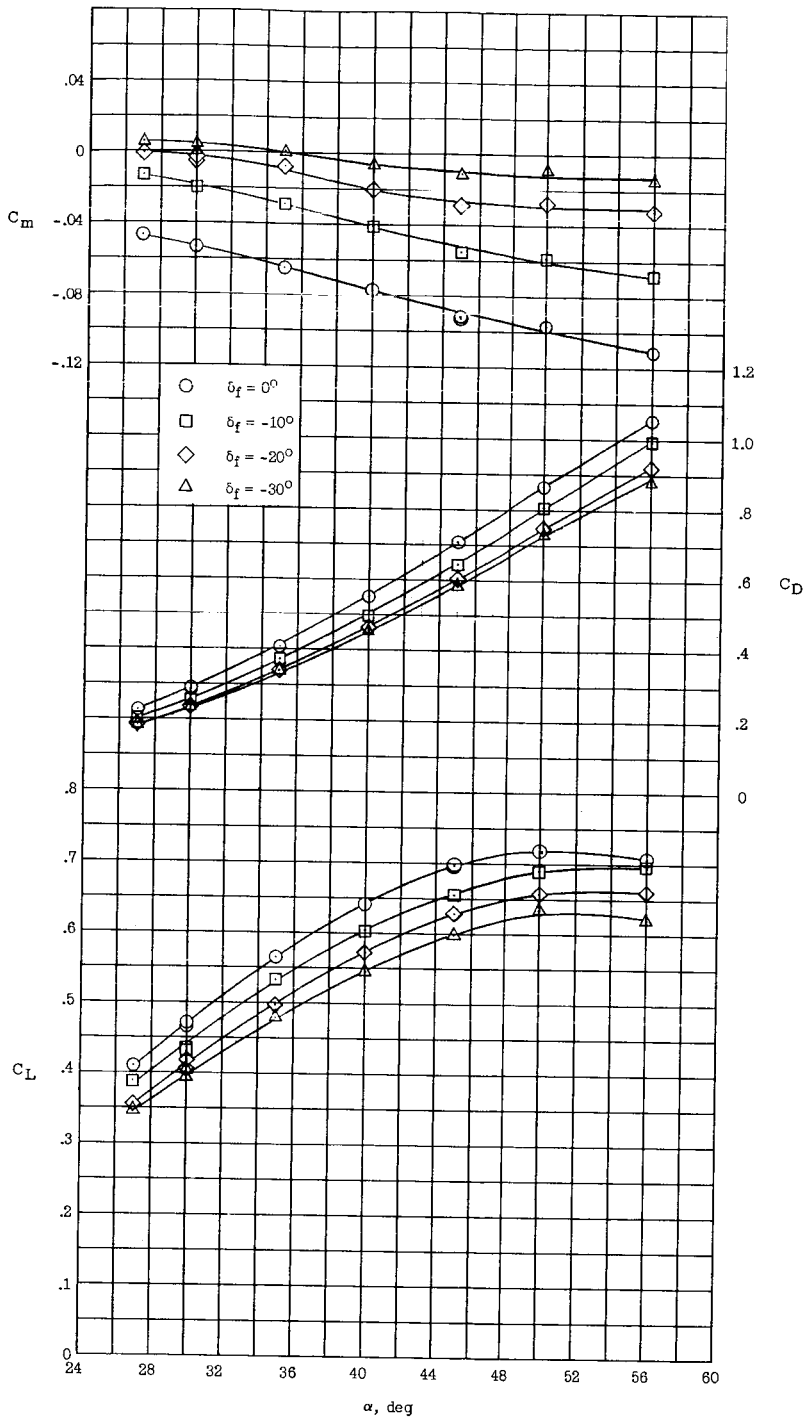


(a) $\delta_n = 0^\circ$; $S_f/S = 0.19$.

Figure 3.- Variation of measured longitudinal stability characteristics with angle of attack for various flap deflections.

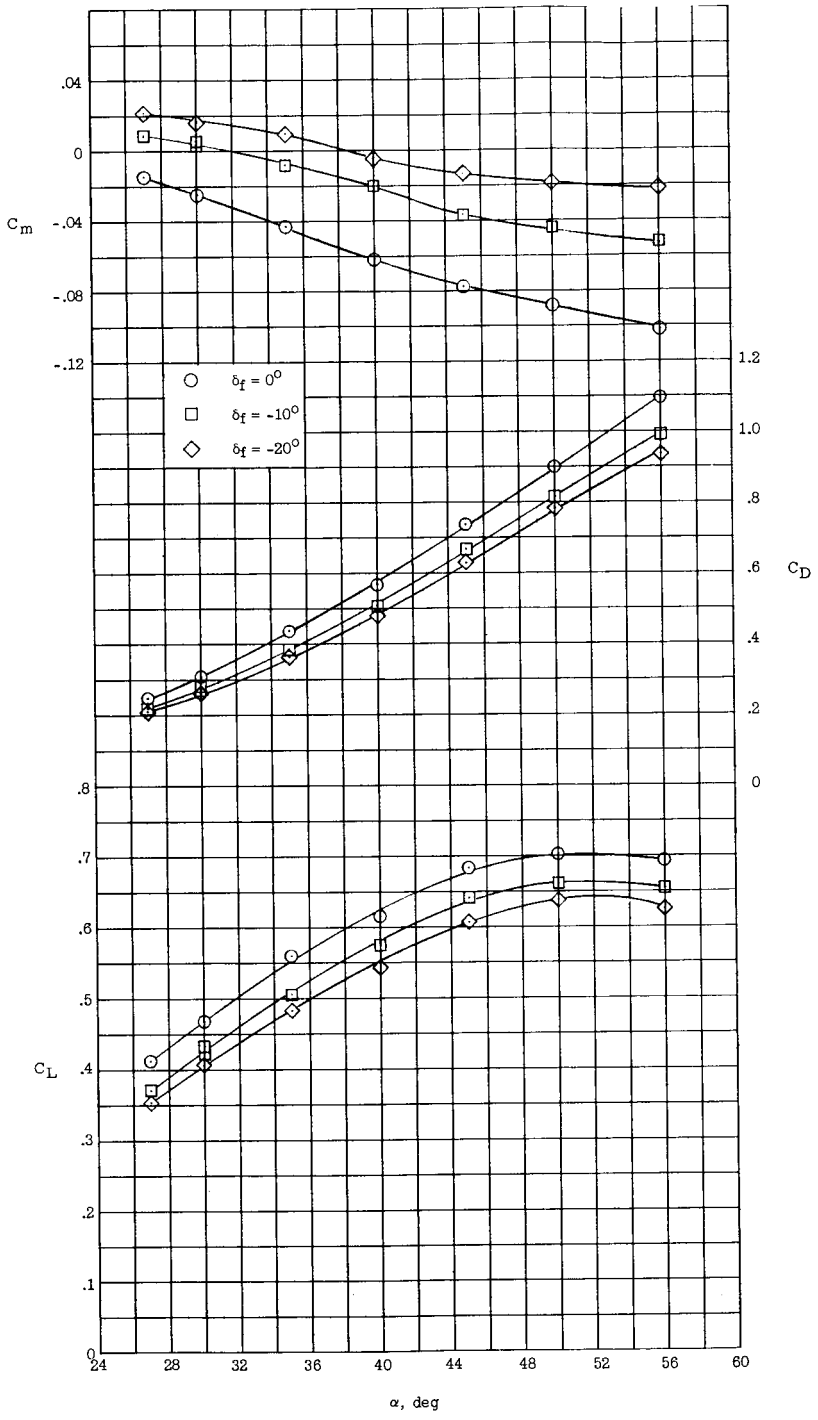


(b) $\delta_n = 10^o$; $S_n/S = 0.16$; $S_f/S = 0.19$.

Figure 3.- Continued.

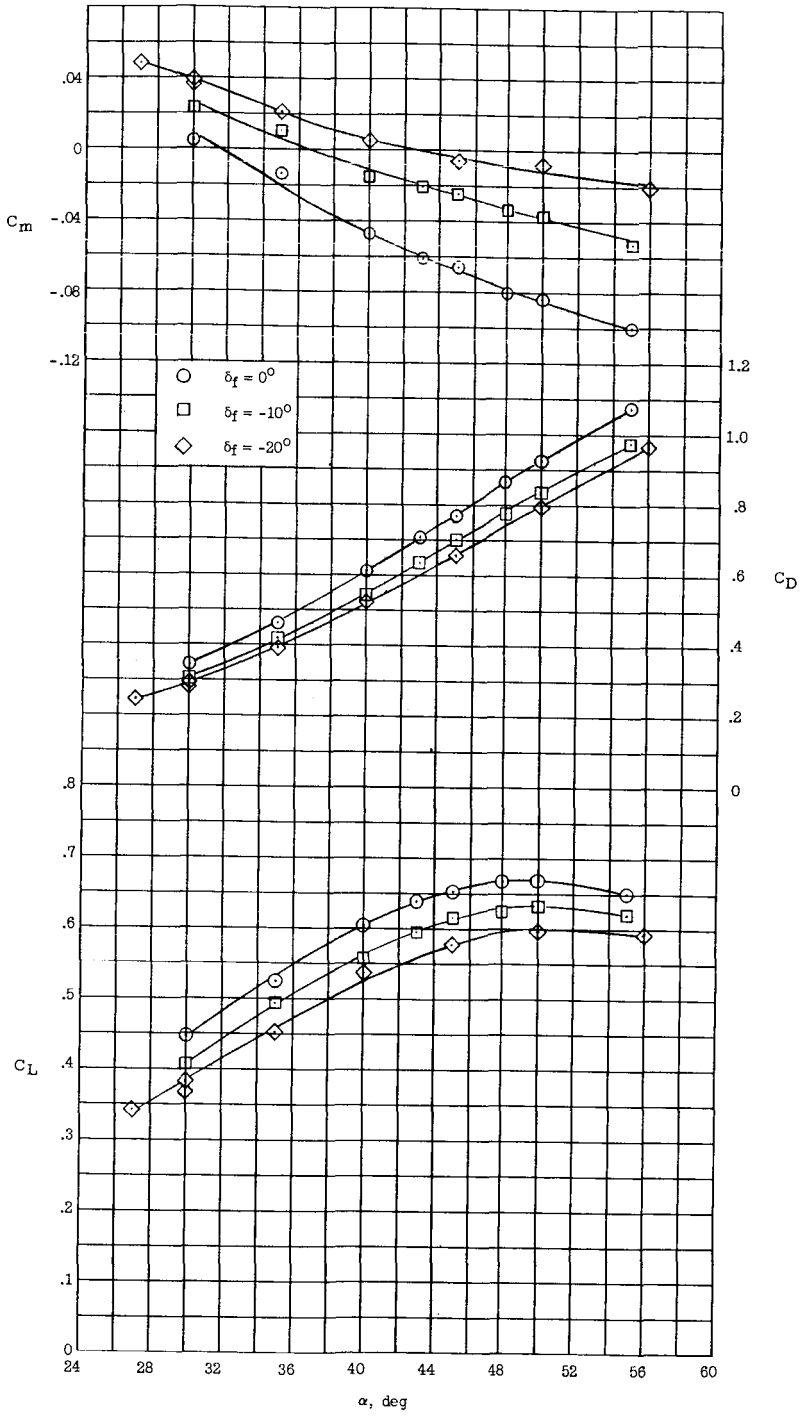


(c) $\delta_n = 20^\circ$; $S_n/S = 0.16$; $S_f/S = 0.19$.

Figure 3.- Continued.

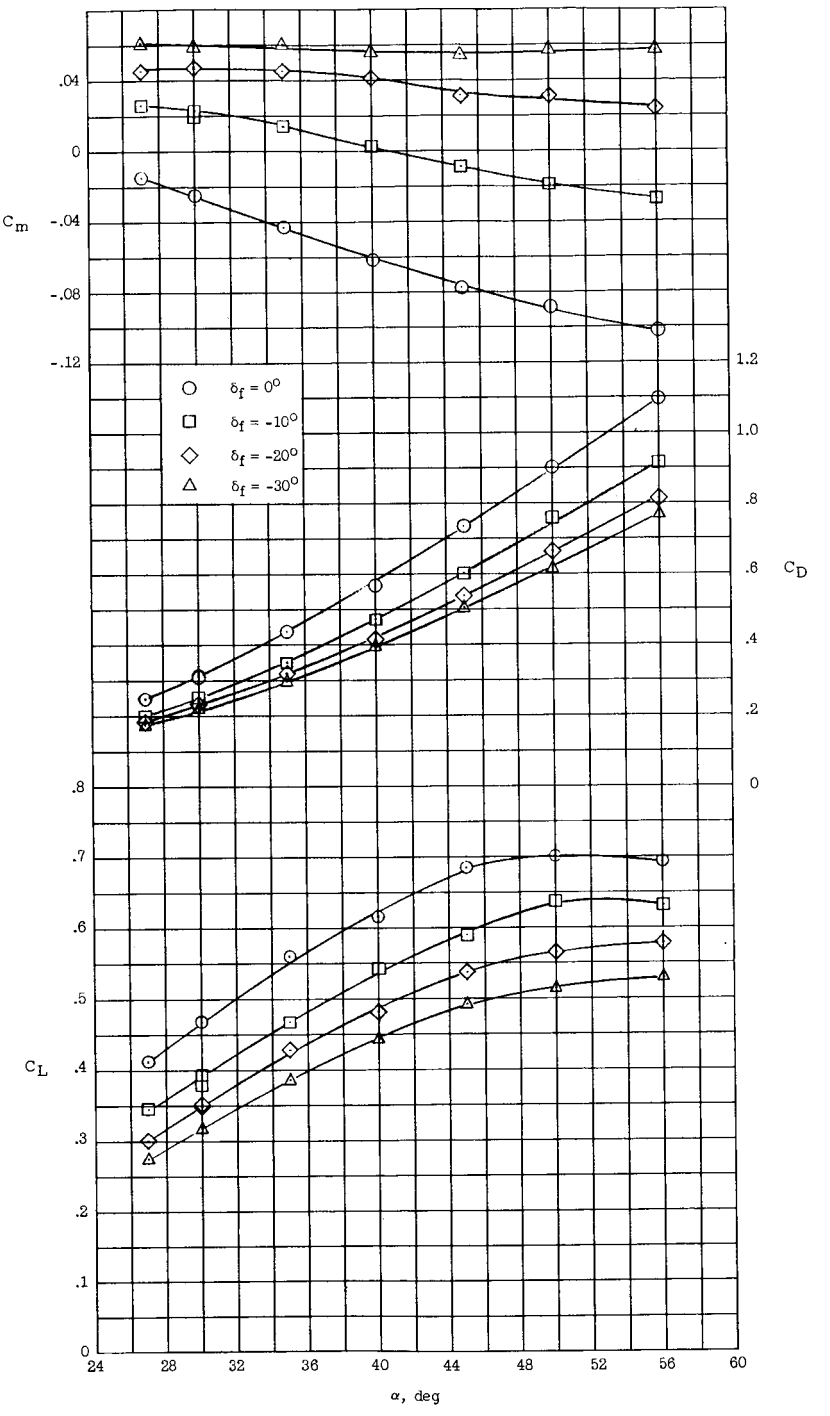


(d) $\delta_n = 10^o$; $S_n/S = 0.16$; $S_f/S = 0.36$.

Figure 3.- Concluded.

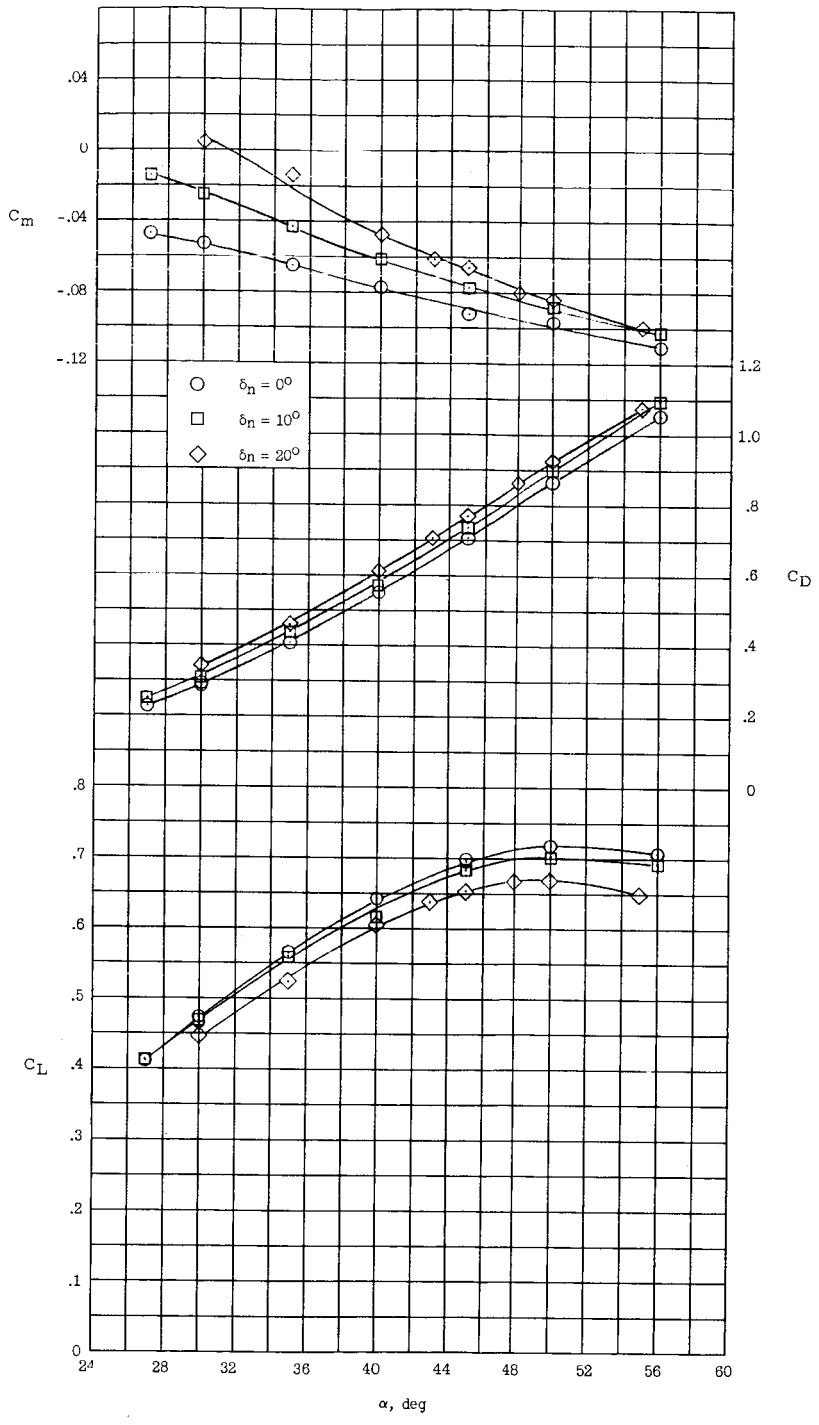


(a) $\delta_f = 0^o$; $S_f/S = 0.19$.

Figure 4.- Variation of measured longitudinal stability characteristics with angle of attack for several nose deflections. $S_n/S = 0.16$.

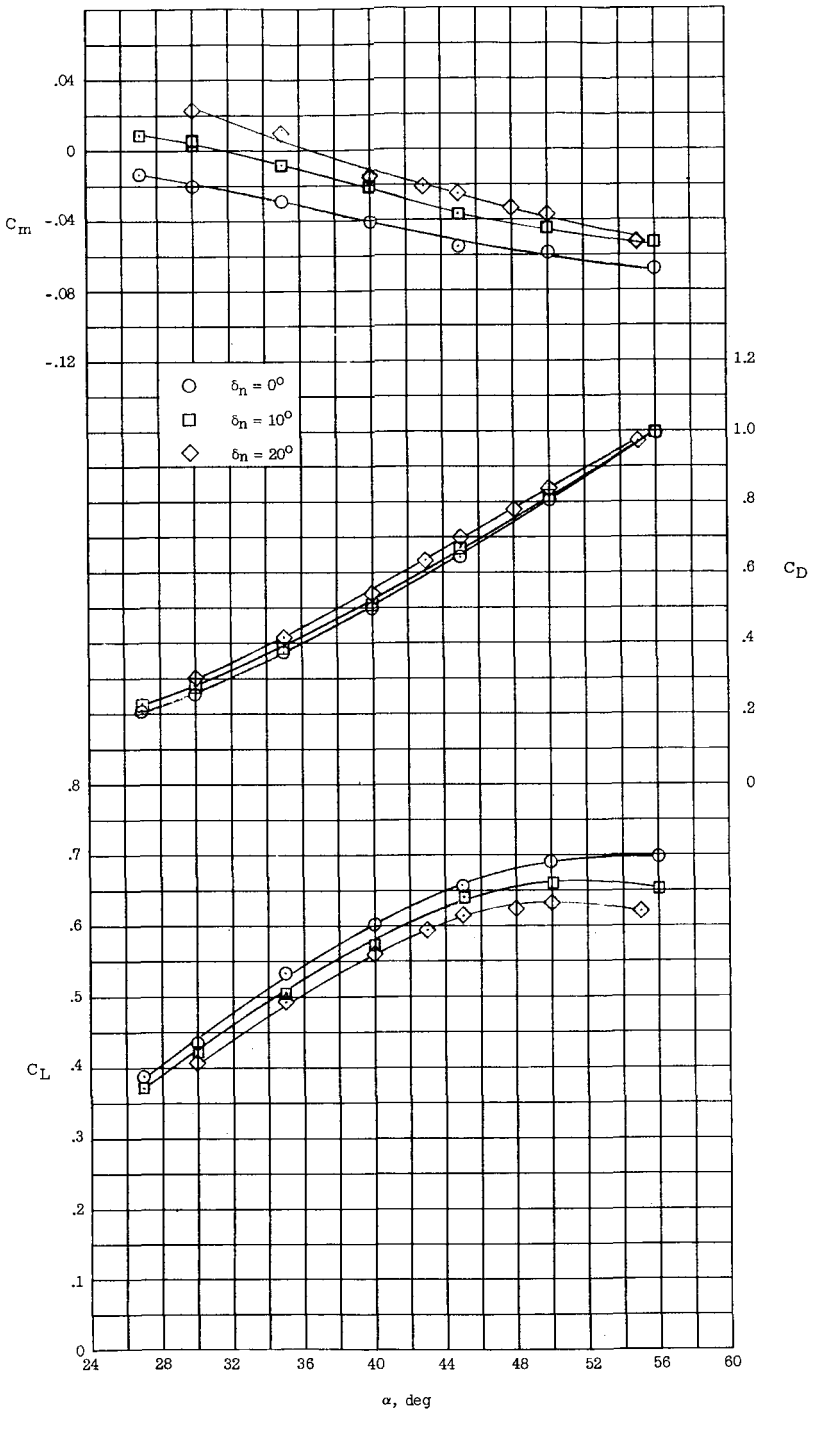


(b) $\delta_f = -10^o$; $S_f/S = 0.19$.

Figure 4.- Continued.

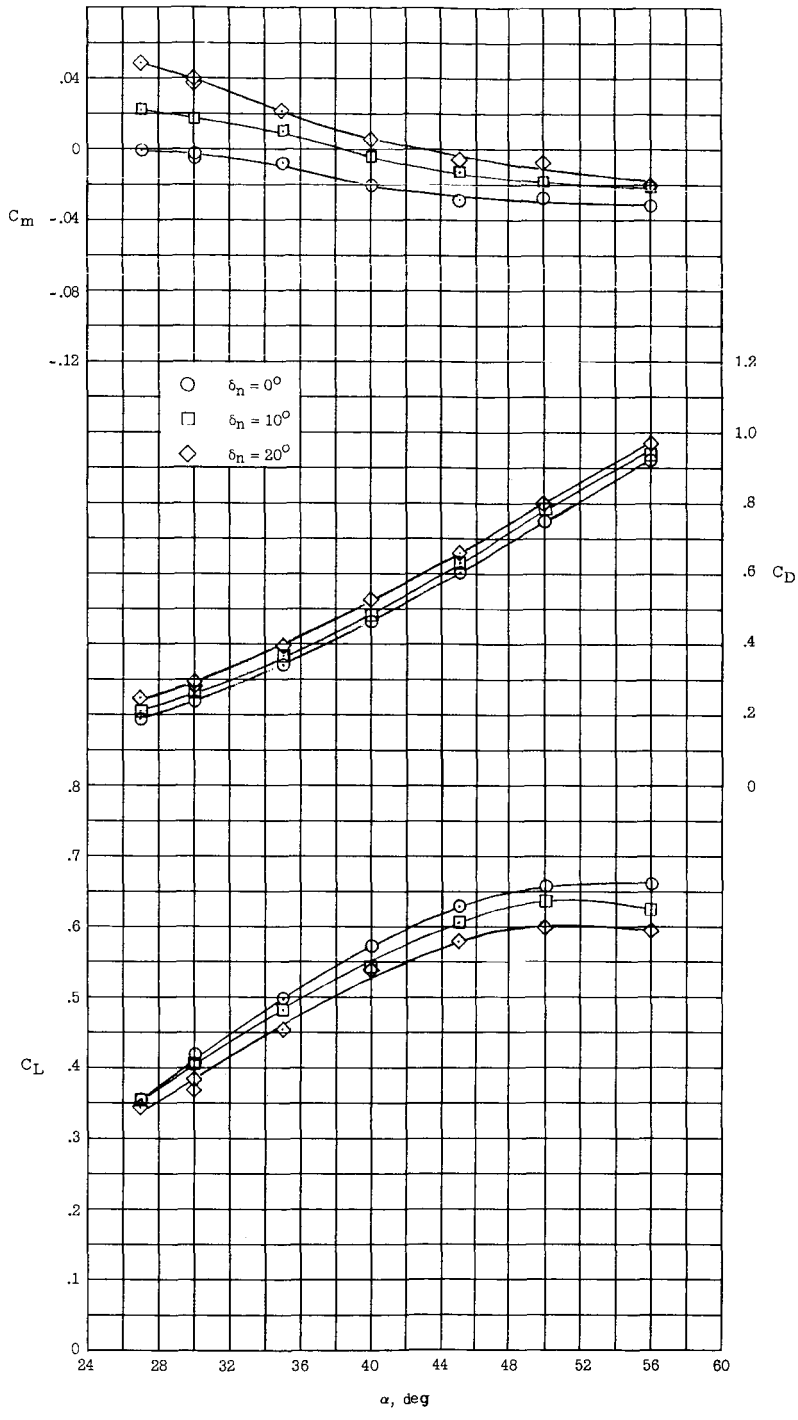


(c) $\delta_f = -20^o$; $S_f/S = 0.19$.

Figure 4.- Concluded.

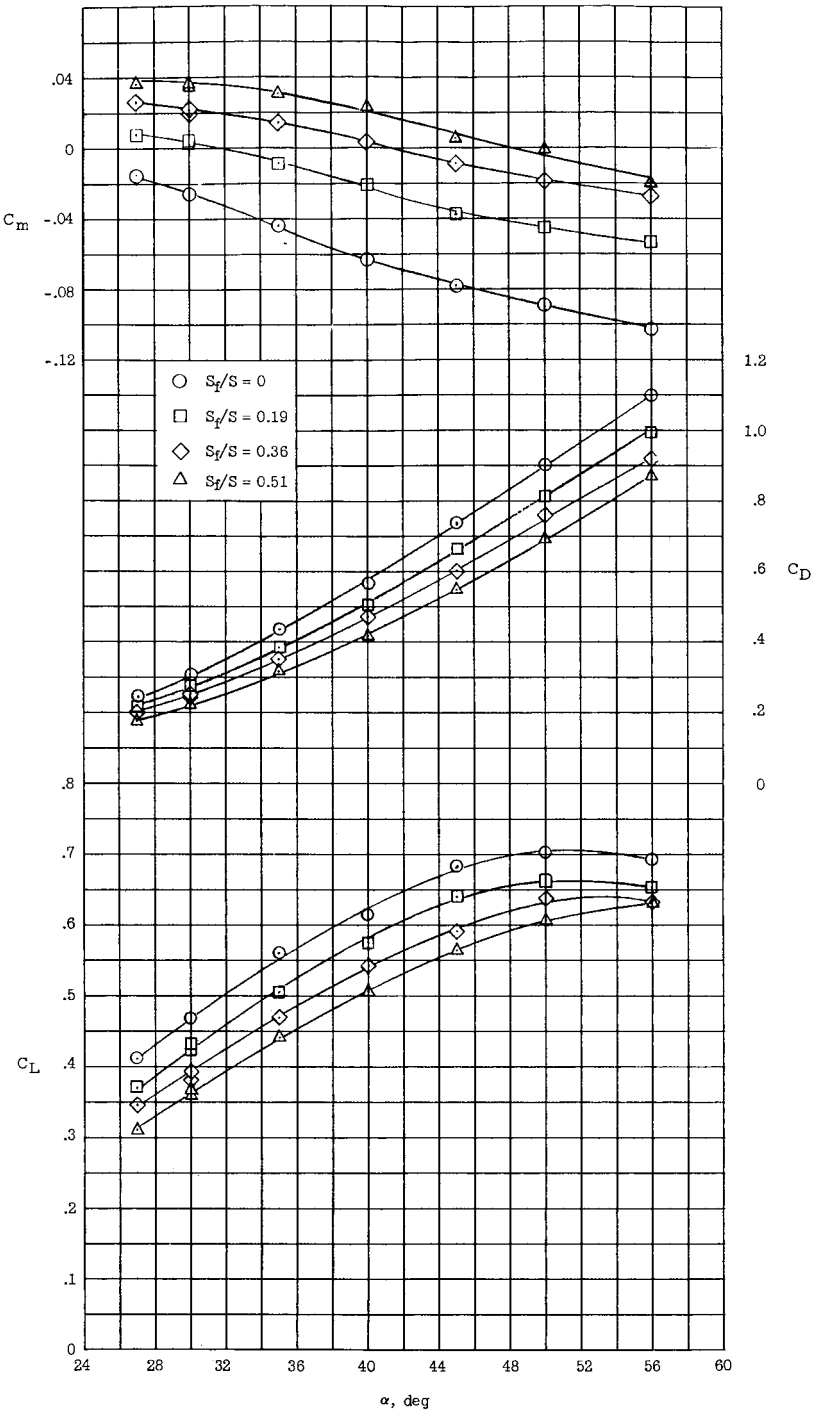


(a) $\delta_n = 10^\circ$; $S_n/S = 0.16$; $\delta_f = -10^\circ$.

Figure 5.- Variation of measured longitudinal stability characteristics with angle of attack for variable flap area with fixed flap deflection.

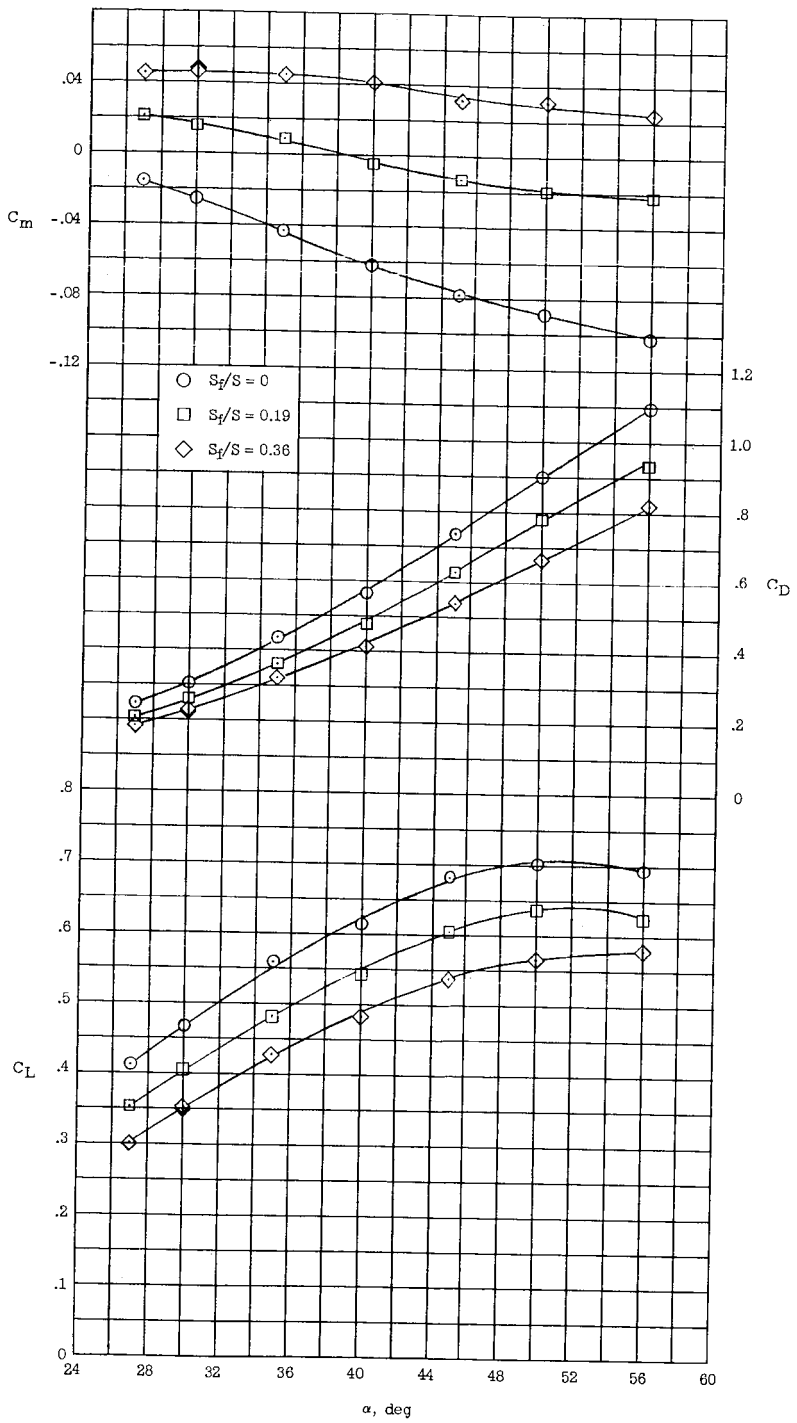


(b) $\delta_n = 10^o$; $S_n/S = 0.16$; $\delta_f = -20^o$.

Figure 5.- Concluded.

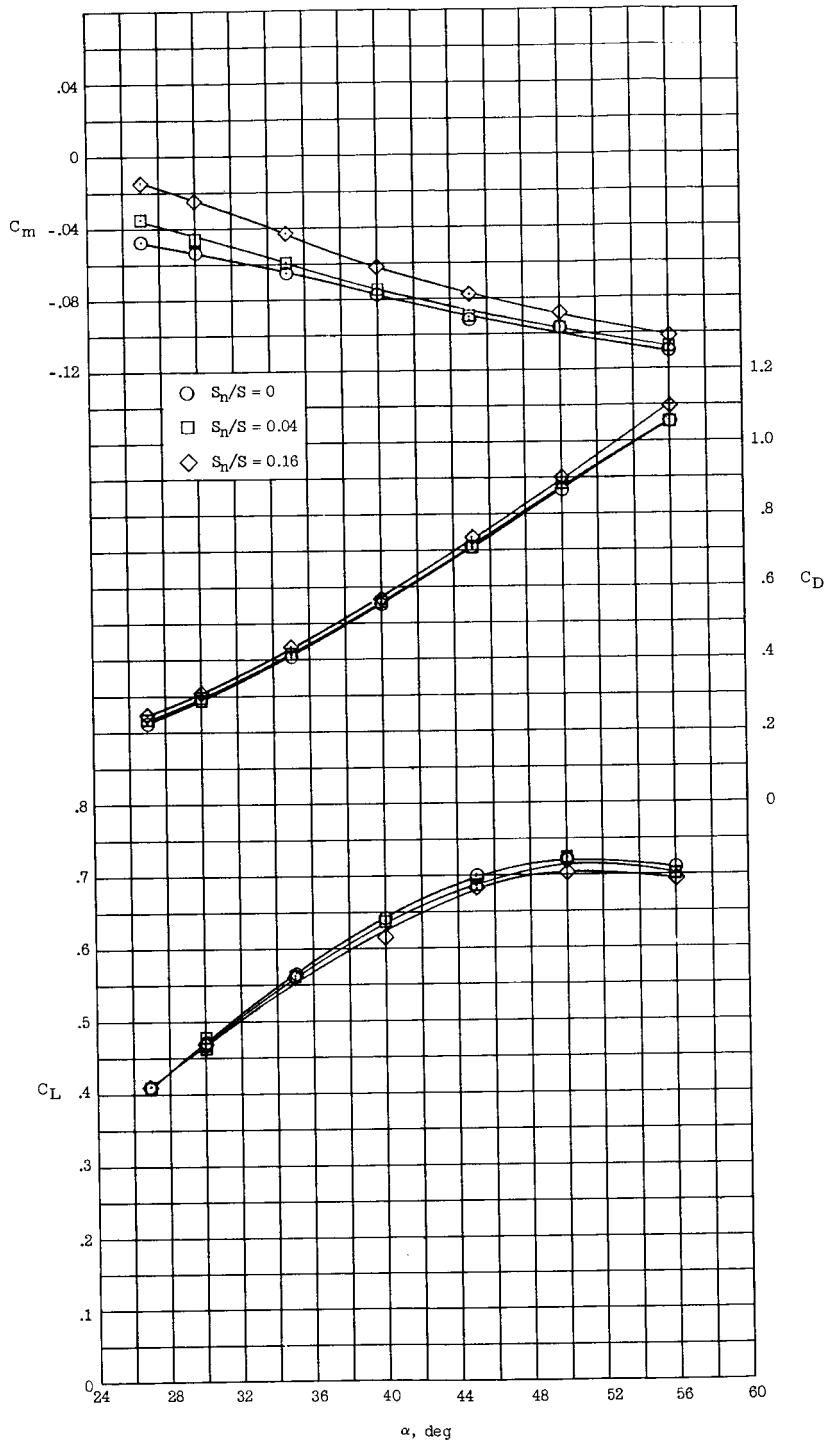


Figure 6.- Variation of measured longitudinal stability characteristics with angle of attack for variable nose area with fixed nose deflection. $\delta_n = 10^o$; $\delta_f = 0^o$.

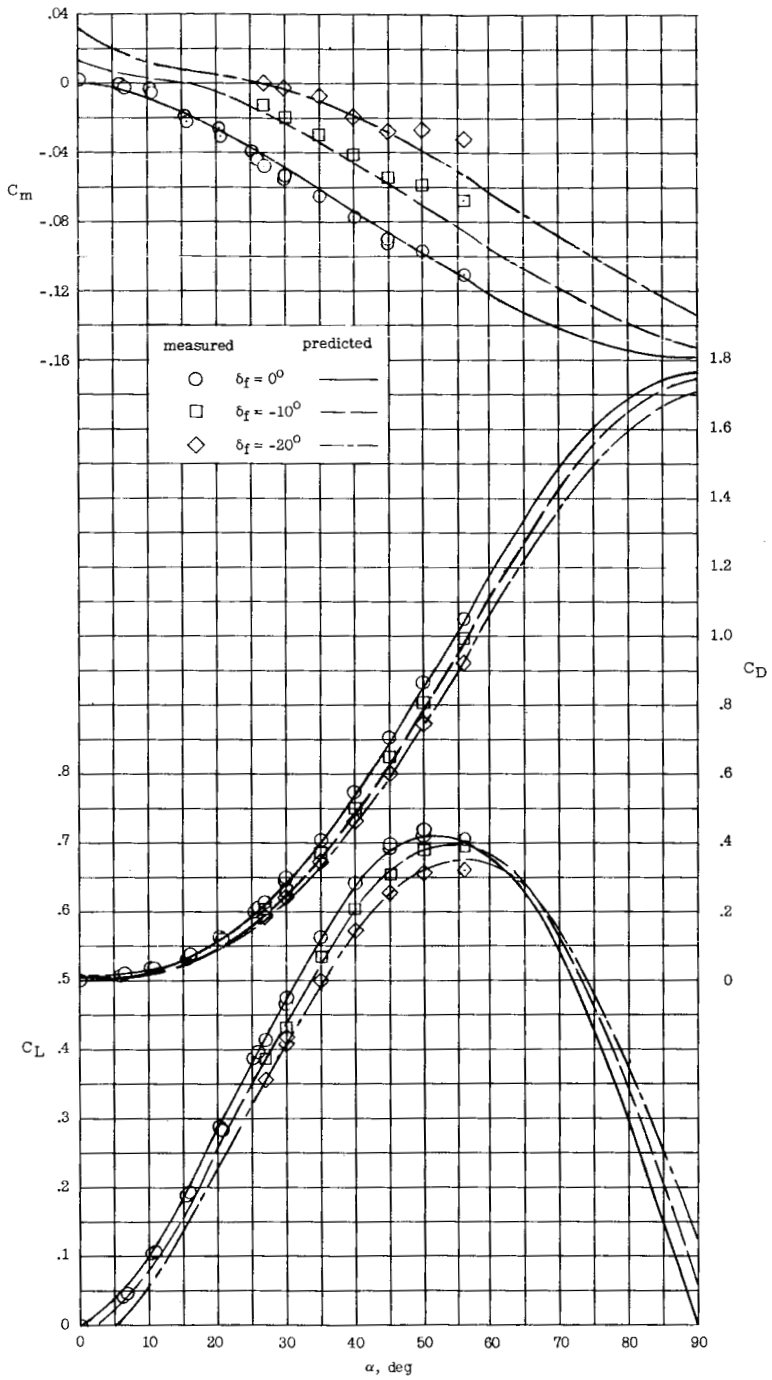


Figure 7.- Variation of measured and predicted longitudinal stability characteristics with angle of attack for various flap deflections. $\delta_n = 0^o$; $S_f/S = 0.19$.

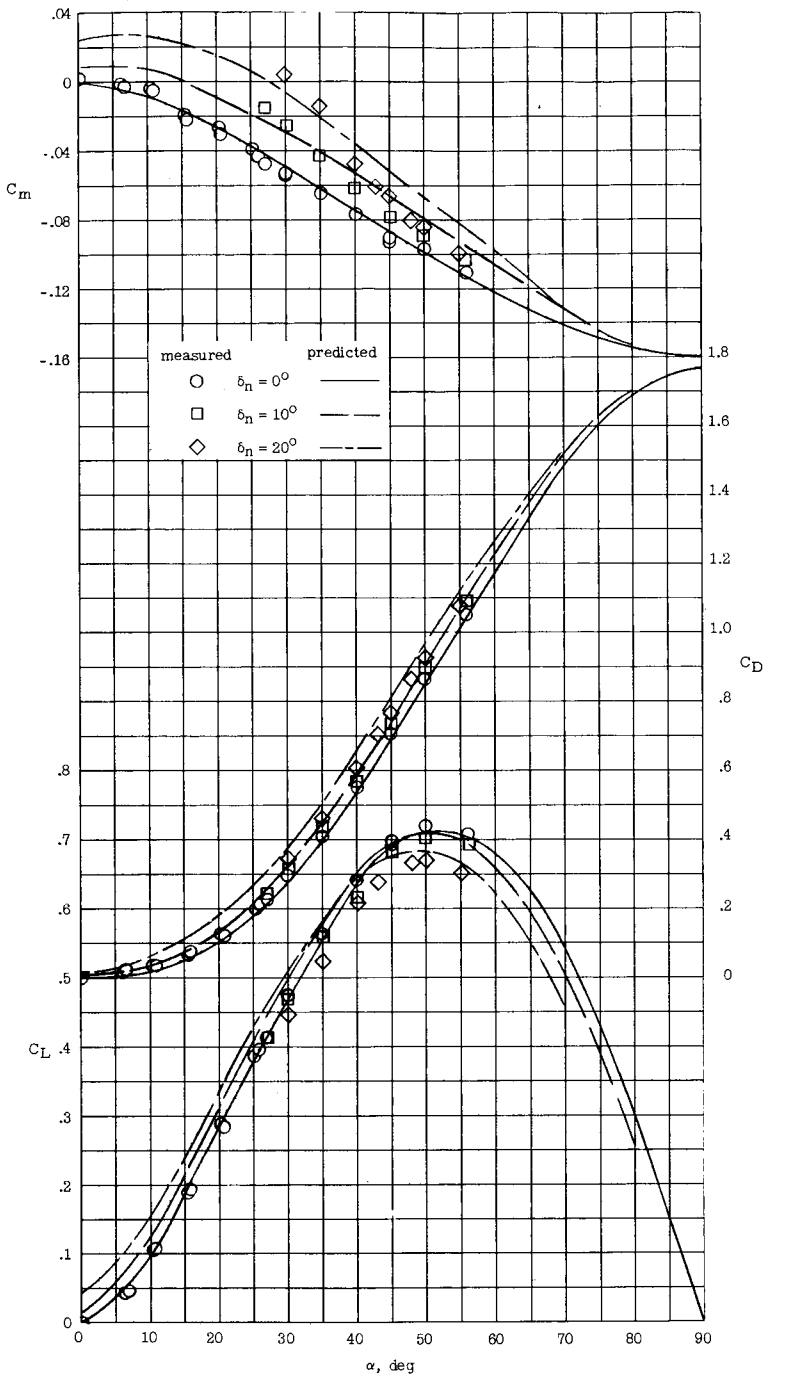


Figure 8.- Variation of measured and predicted longitudinal stability characteristics with angle of attack for various nose deflections. $\delta_f = 0^o$; $S_n/S = 0.16$.

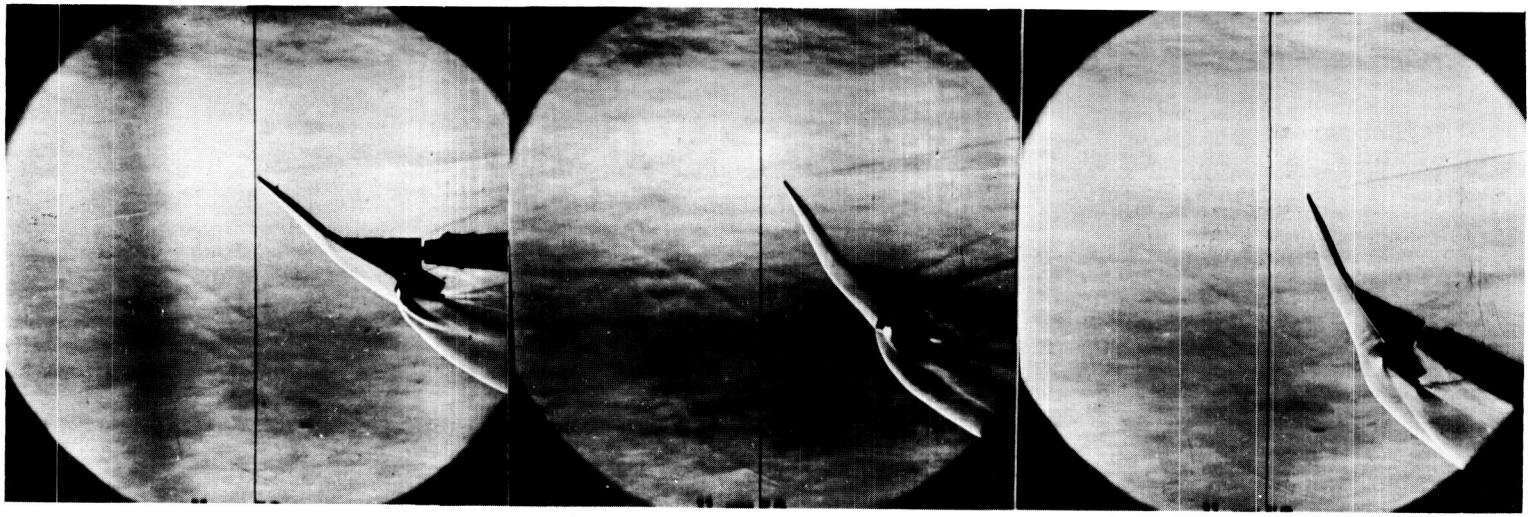

$\alpha = 30^\circ$ $\alpha = 45^\circ$ $\alpha = 56^\circ$

(a) Wing U-R; $\delta_n = 10^\circ$; $\delta_f = -20^\circ$. L-59-8201

Figure 9.- Schlieren photographs of two models at various angles of attack.

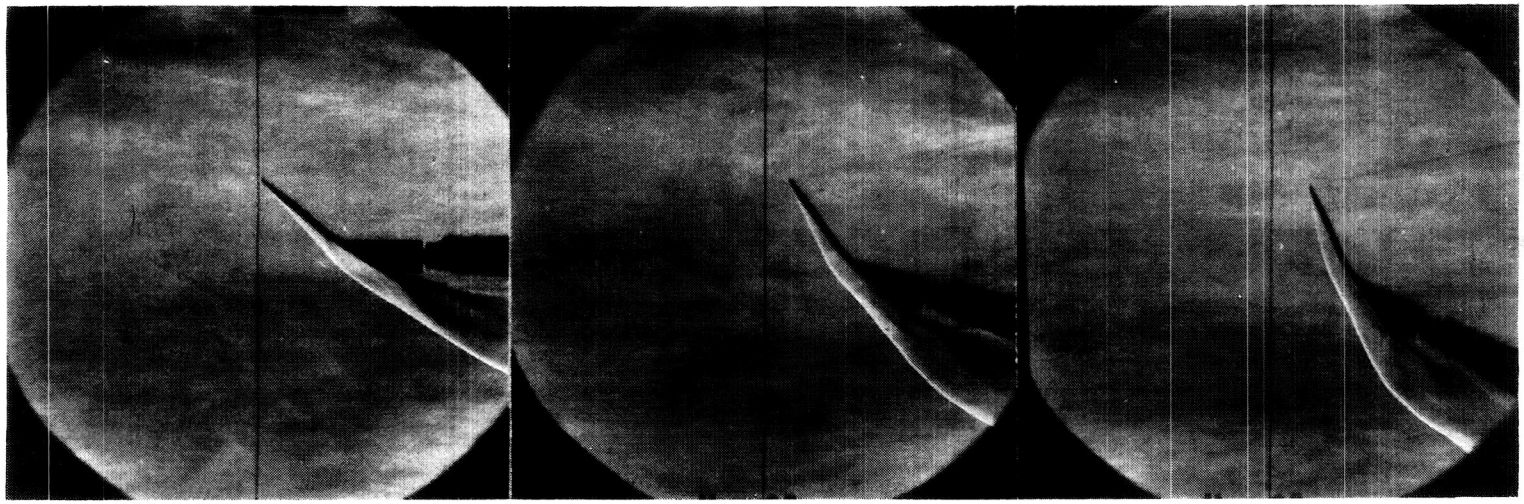

$\alpha = 30^\circ$ $\alpha = 45^\circ$ $\alpha = 56^\circ$

(b) Wing 3; $\delta_n = 10^\circ$; $\delta_f = -20^\circ$. L-59-8202

Figure 9.- Concluded.

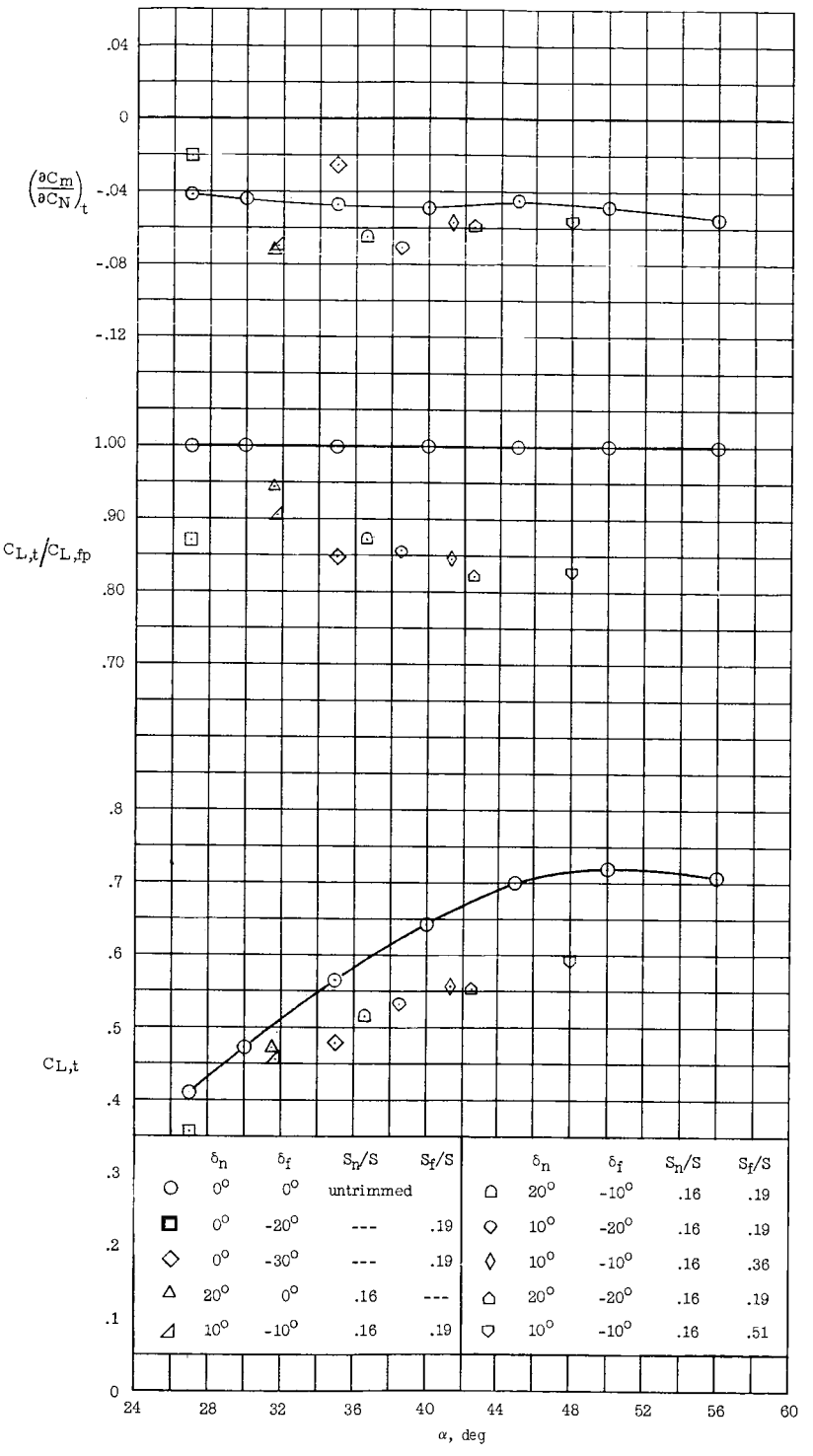


Figure 10.- Measured trimmed characteristics with center of gravity at 0.42$\bar{c}$.

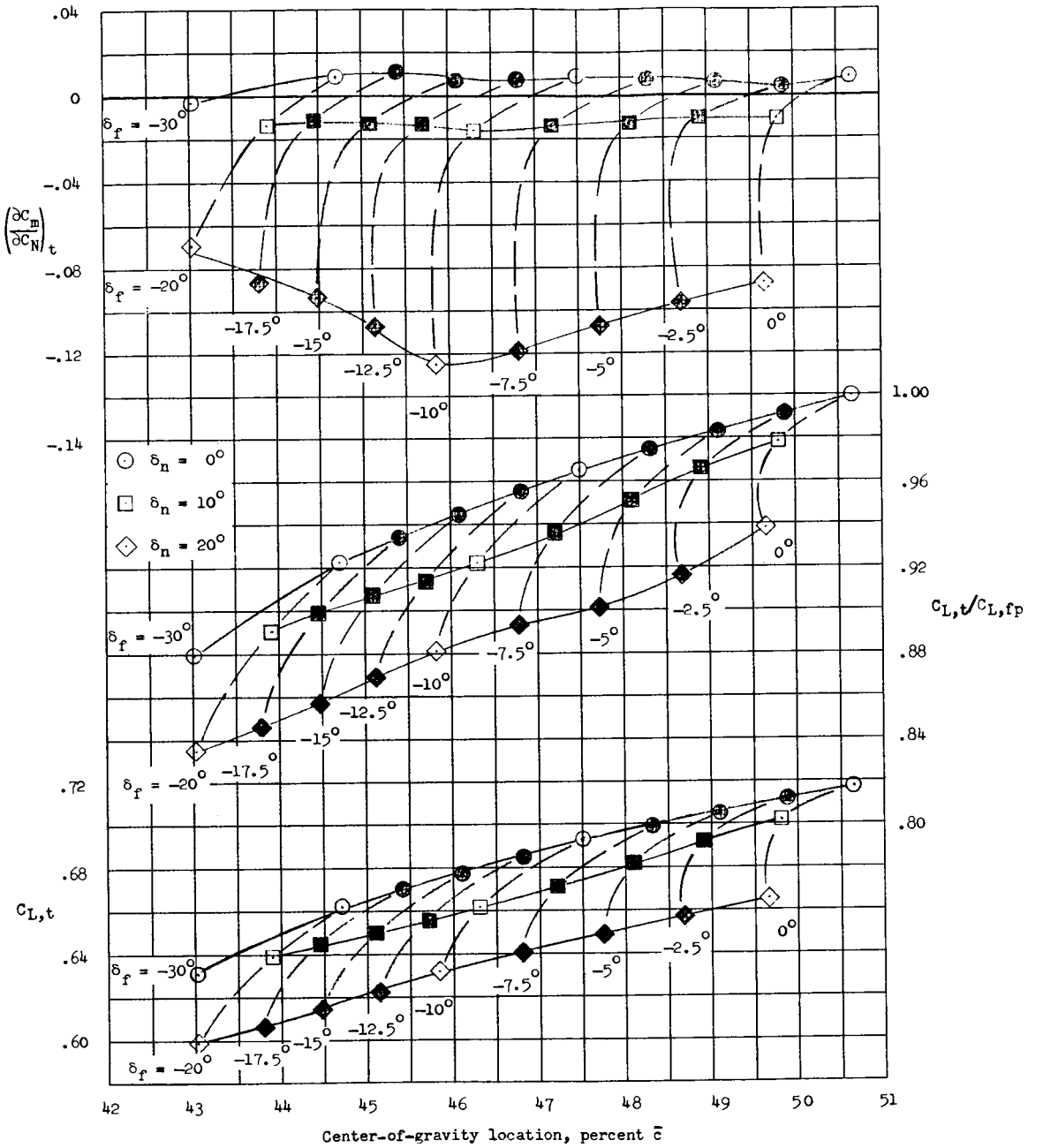


Figure 11.- Effect of center-of-gravity location on trimmed characteristics at $\alpha = 52^{\circ}$. (Dashed lines are lines of constant flap deflection.) $S_n/S = 0.16$; $S_f/S = 0.19$.

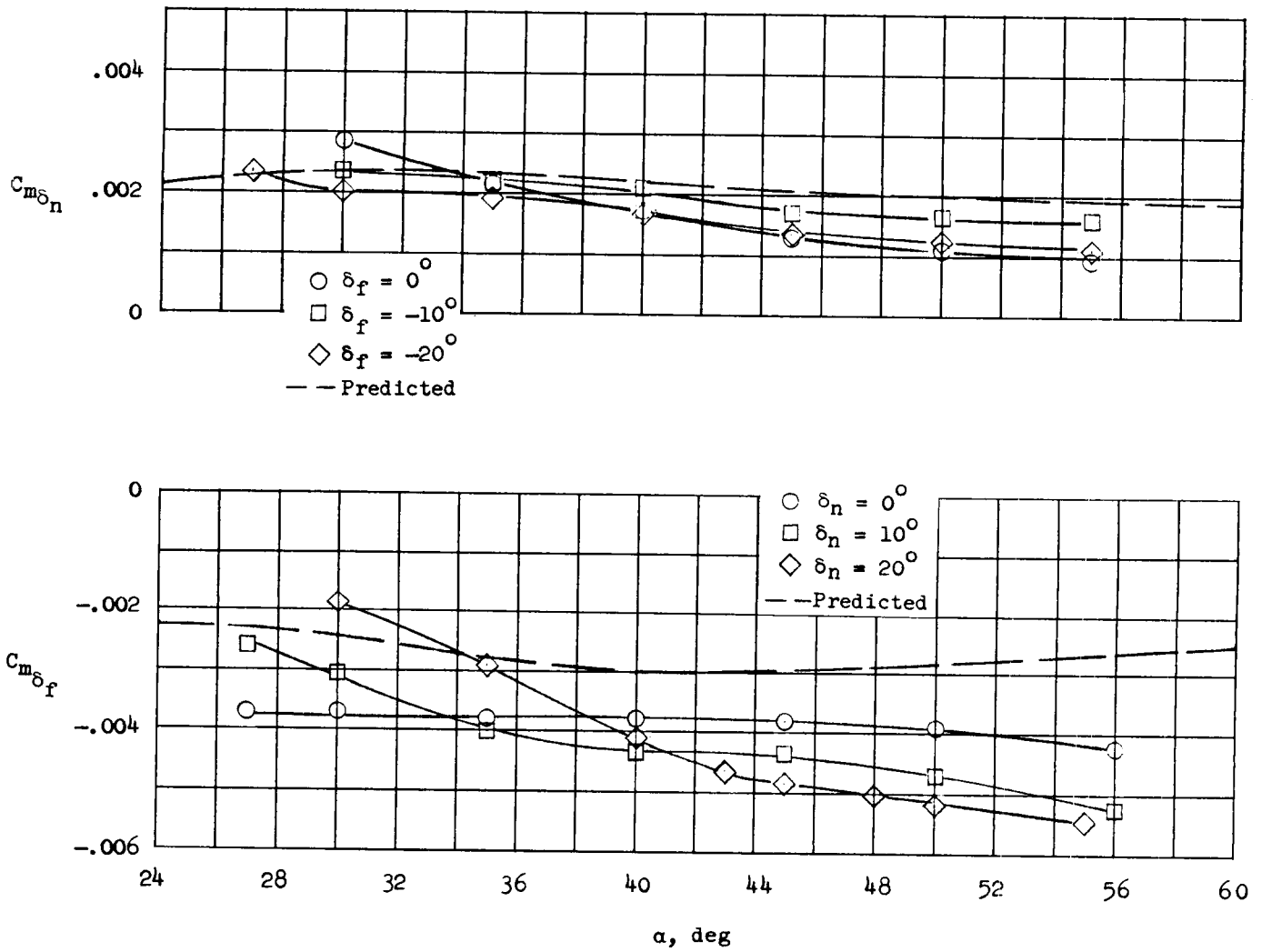


Figure 12.- Variation of nose- and flap-control effectiveness derivatives with angle of attack. $S_n/S = 0.16$; $S_f/S = 0.19$.

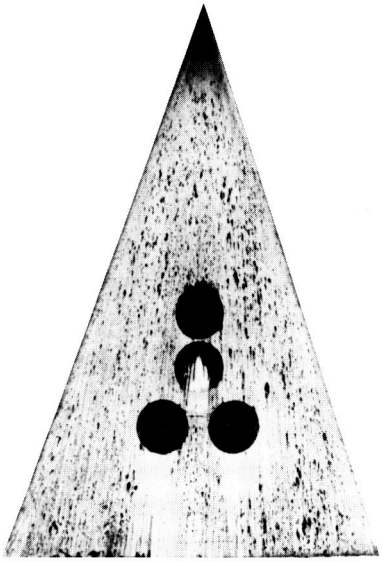

$\delta_n = 0^\circ$ ; $\delta_f = 0^\circ$

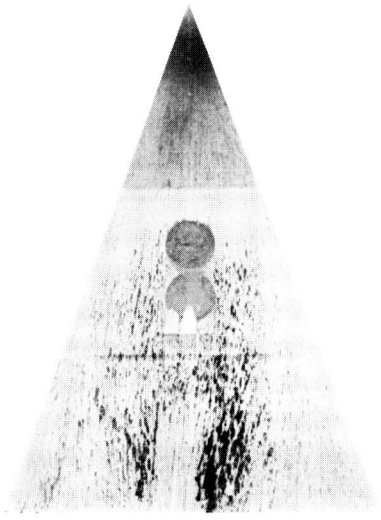

$\delta_n = 10^\circ$ ; $\delta_f = 0^\circ$

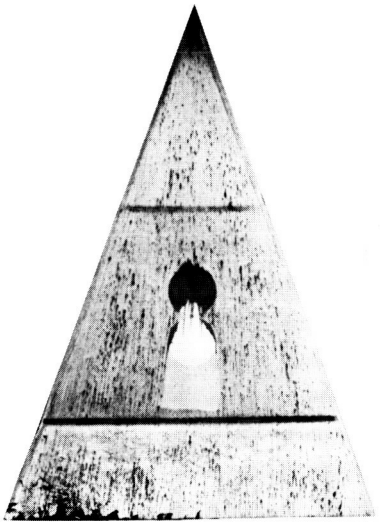

$\delta_n = 0^\circ$ ; $\delta_f = -10^\circ$

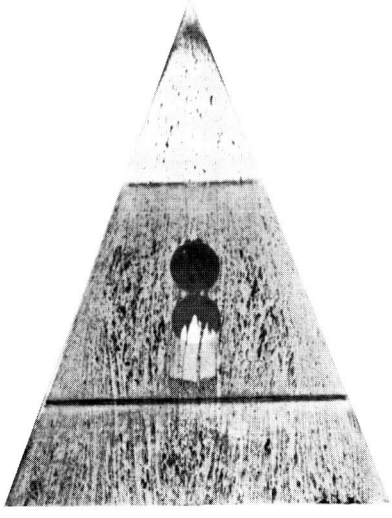

$\delta_n = 10^\circ$ ; $\delta_f = -10^\circ$

L-59-8203

Figure 13.- Carbon-black and oil streak photographs showing the effect of nose deflection on local flow direction. $\alpha = 30^\circ$; $M_\infty = 9.6$.

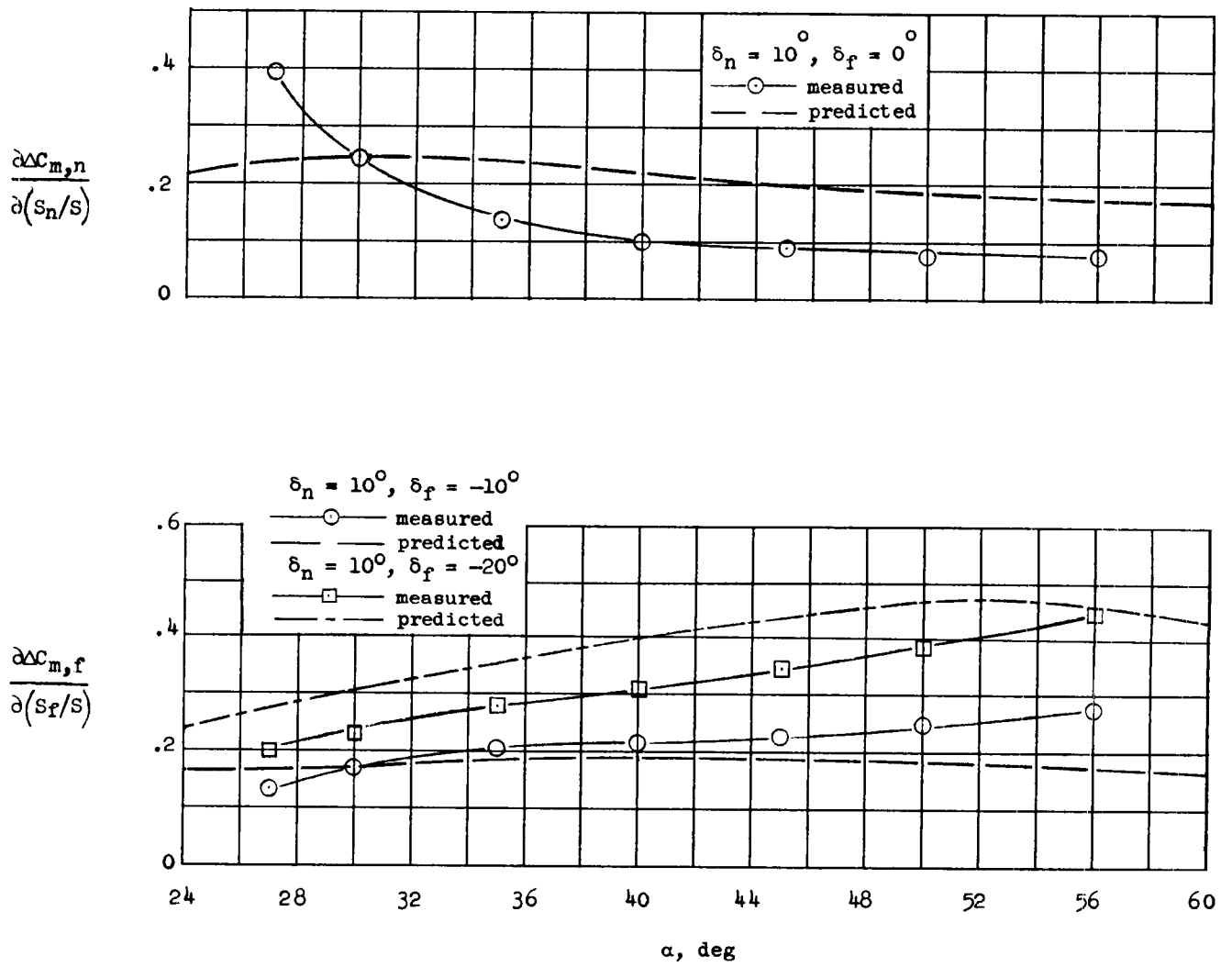


Figure 14.- Variation of nose- and flap-control-area effectiveness derivatives with angle of attack.

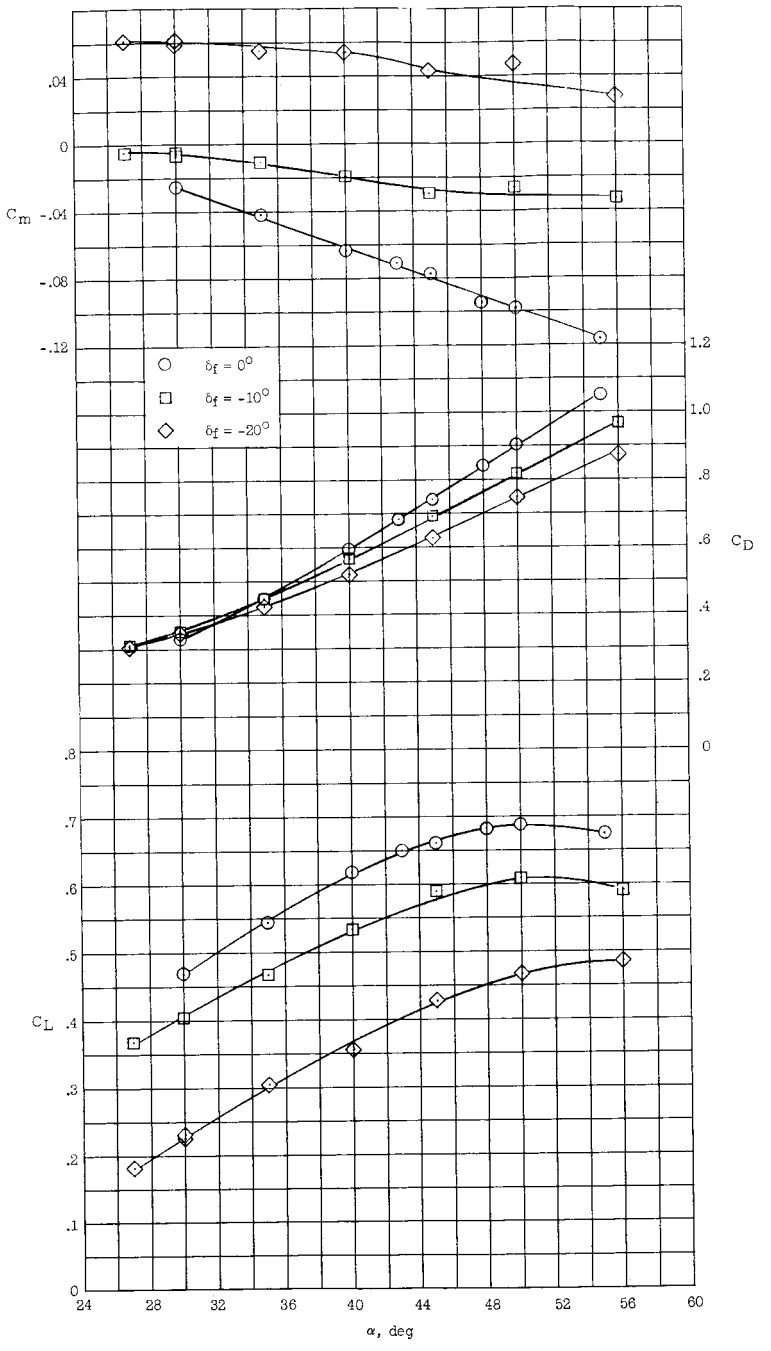


(a) Wing U-R.

Figure 15.- Variations in the longitudinal stability characteristics with angle of attack for several unported flap deflections. $\delta_n = 10^\circ$; $S_n/S = 0.16$; $S_f/S = 0.36$.

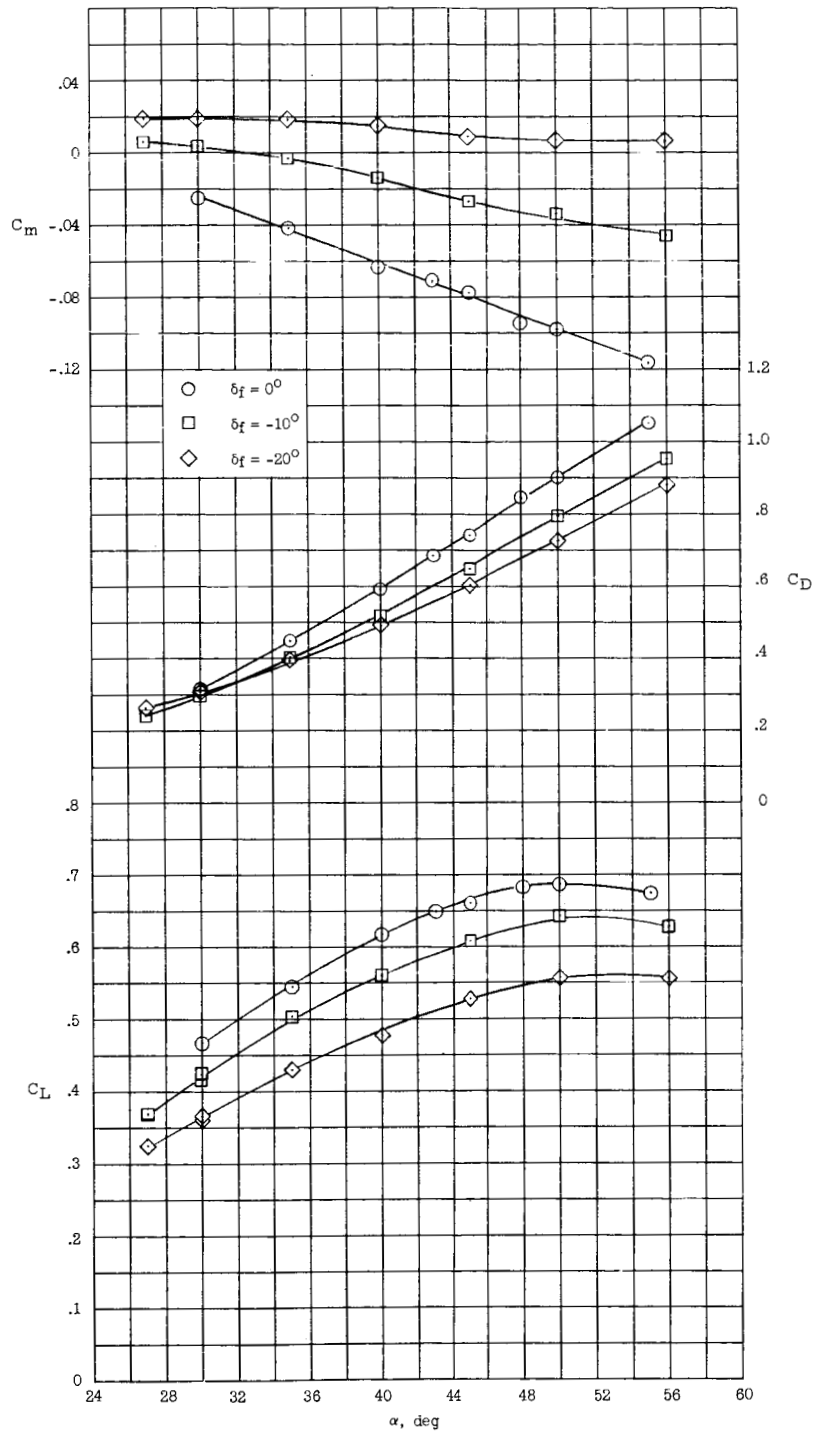


(b) Wing U-C.

Figure 15.- Continued.

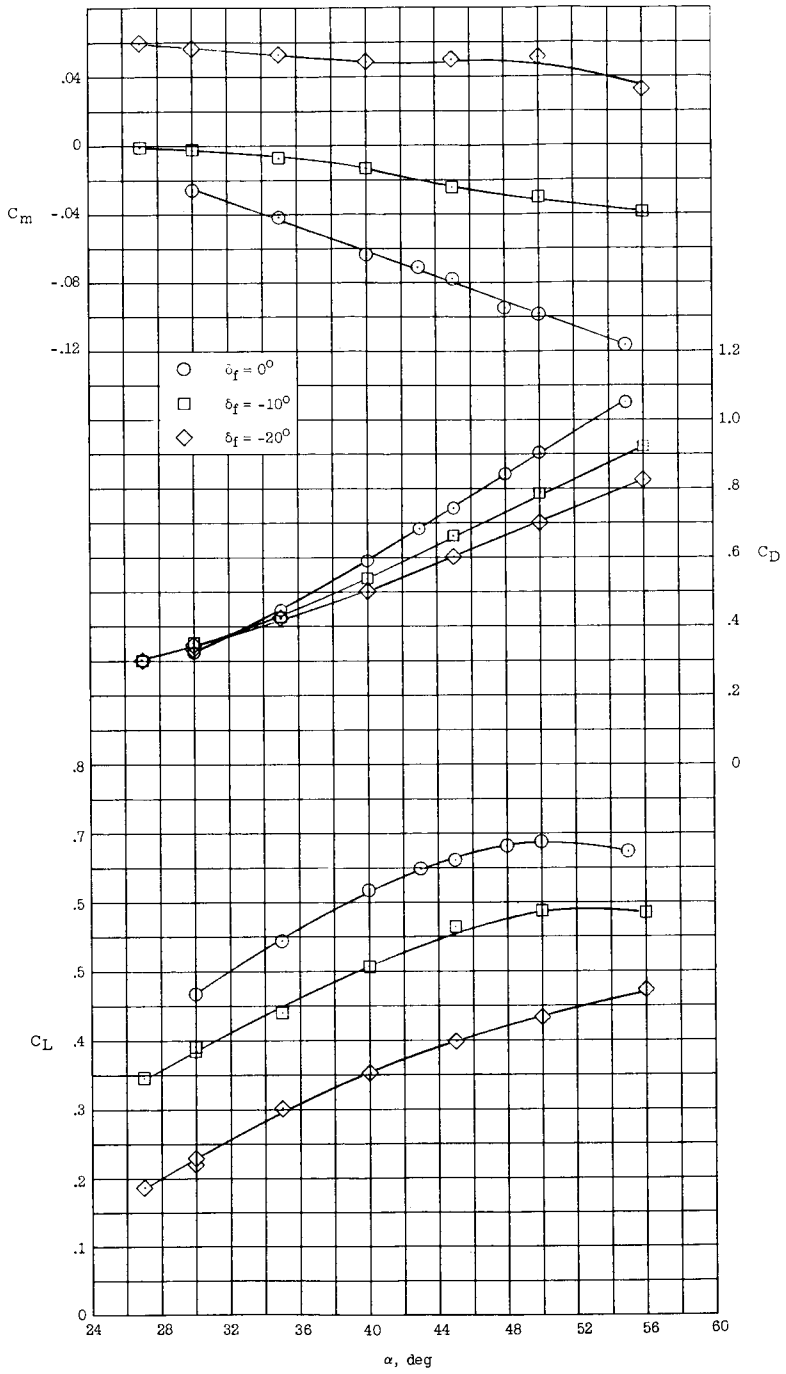


(c) Wing U-Rm.

Figure 15.- Continued.

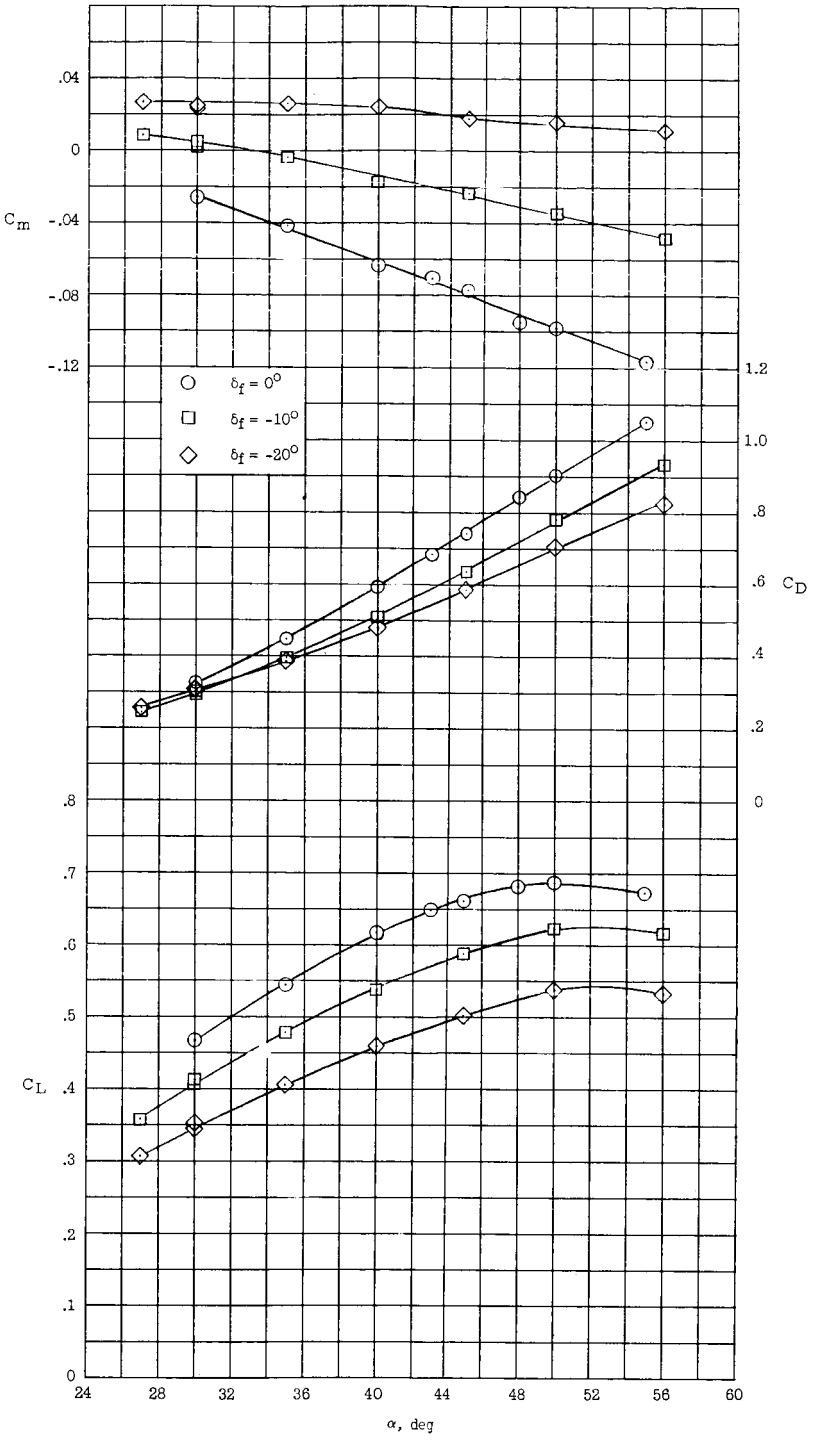


(d) Wing U-Cm.

Figure 15.- Concluded.

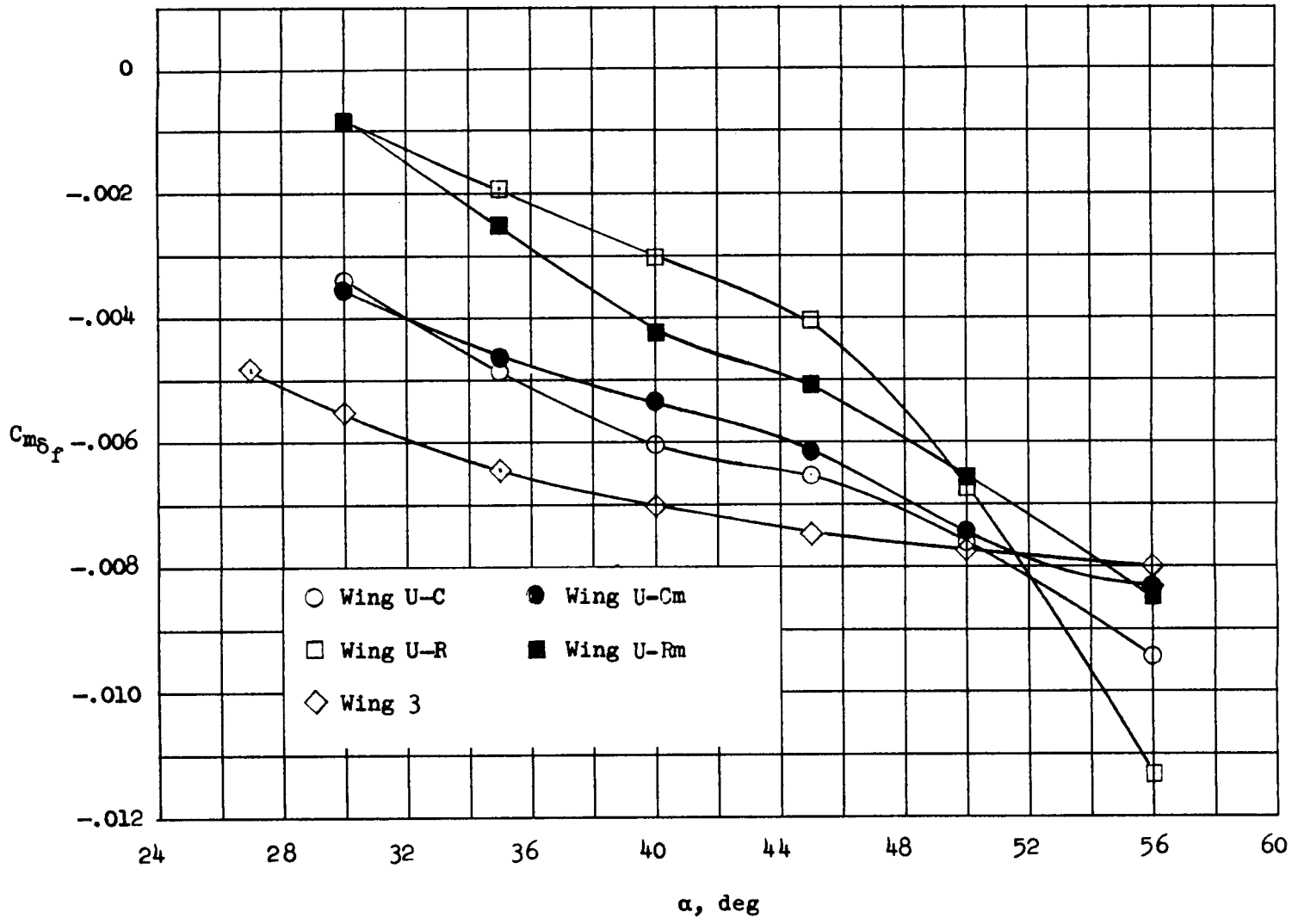


Figure 16.- Variation of flap effectiveness derivatives with angle of attack for four unported flaps and one smooth-bottom flap. $\delta_n = 10^\circ$; $S_n/S = 0.16$; $S_f/S = 0.36$.

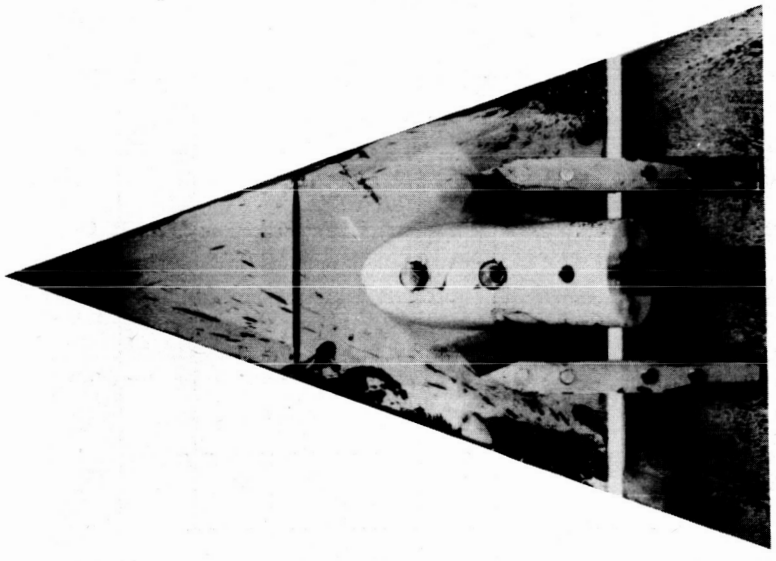

low-pressure side

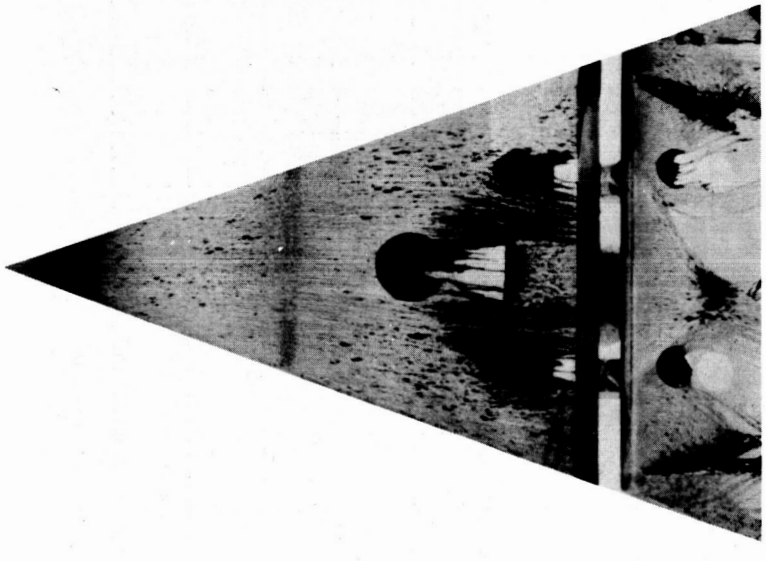

high-pressure side

L-59-8204

Figure 17.- Carbon-black and oil streak photographs showing the complicated flow pattern on an unported flap. $\alpha = 30^{\circ}$; $\delta_n = 10^{\circ}$; $\delta_f = -20^{\circ}$; $M_\infty = 9.6$.

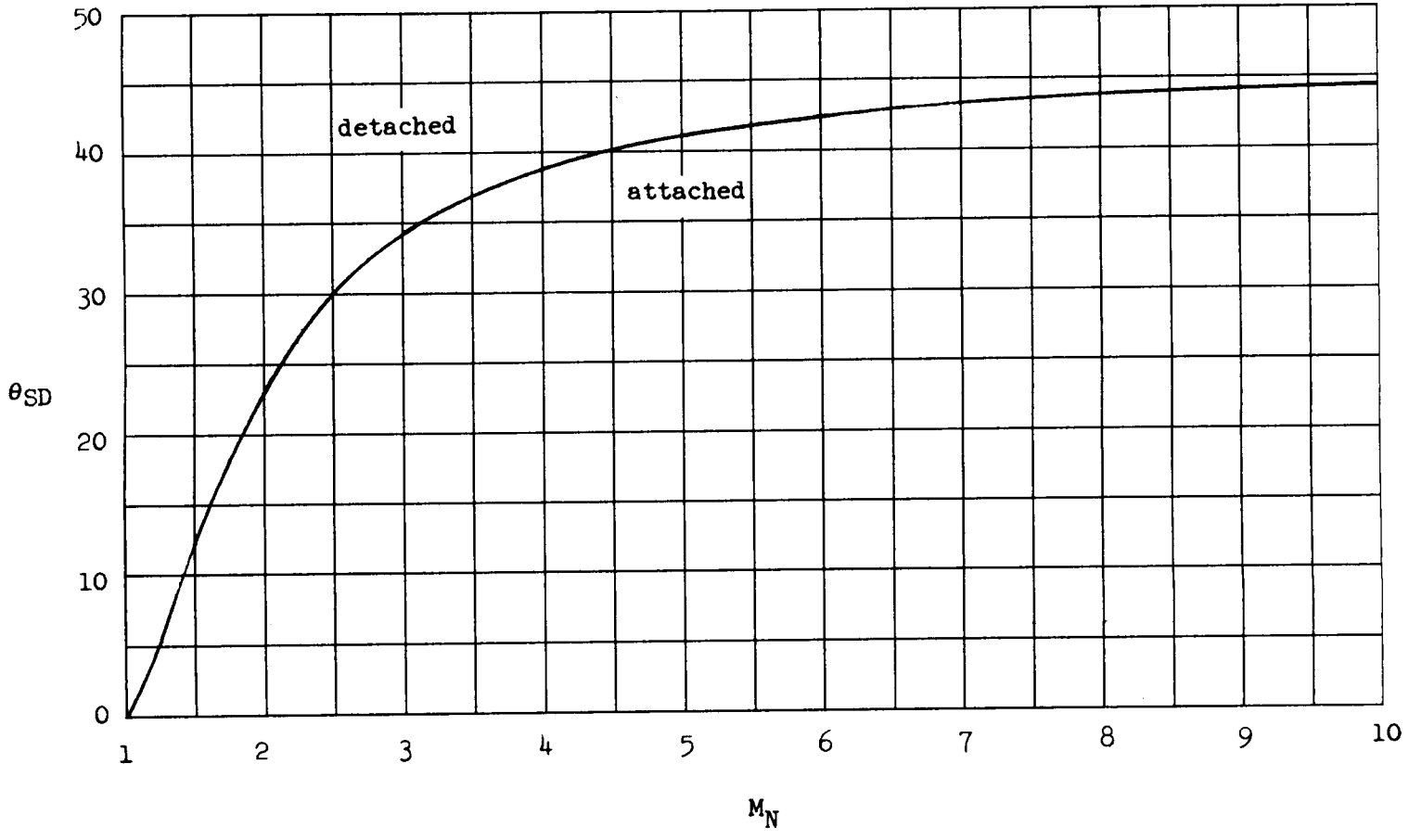


Figure 18.- Variation of shock detachment angle with normal Mach number (from ref. 7 or 8).

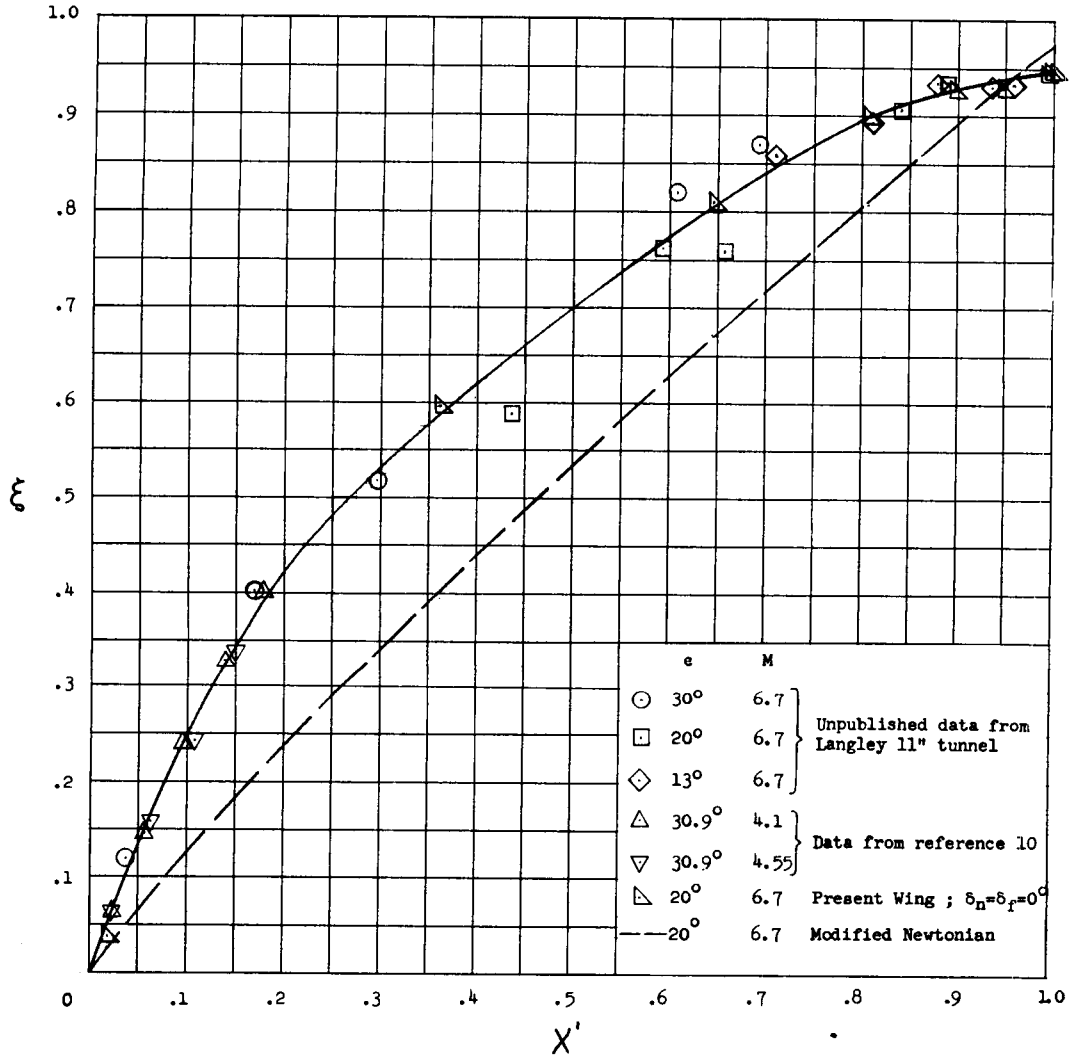


Figure 19.- Empirical normal-force correlation curve compared with modified Newtonian prediction for present wing.

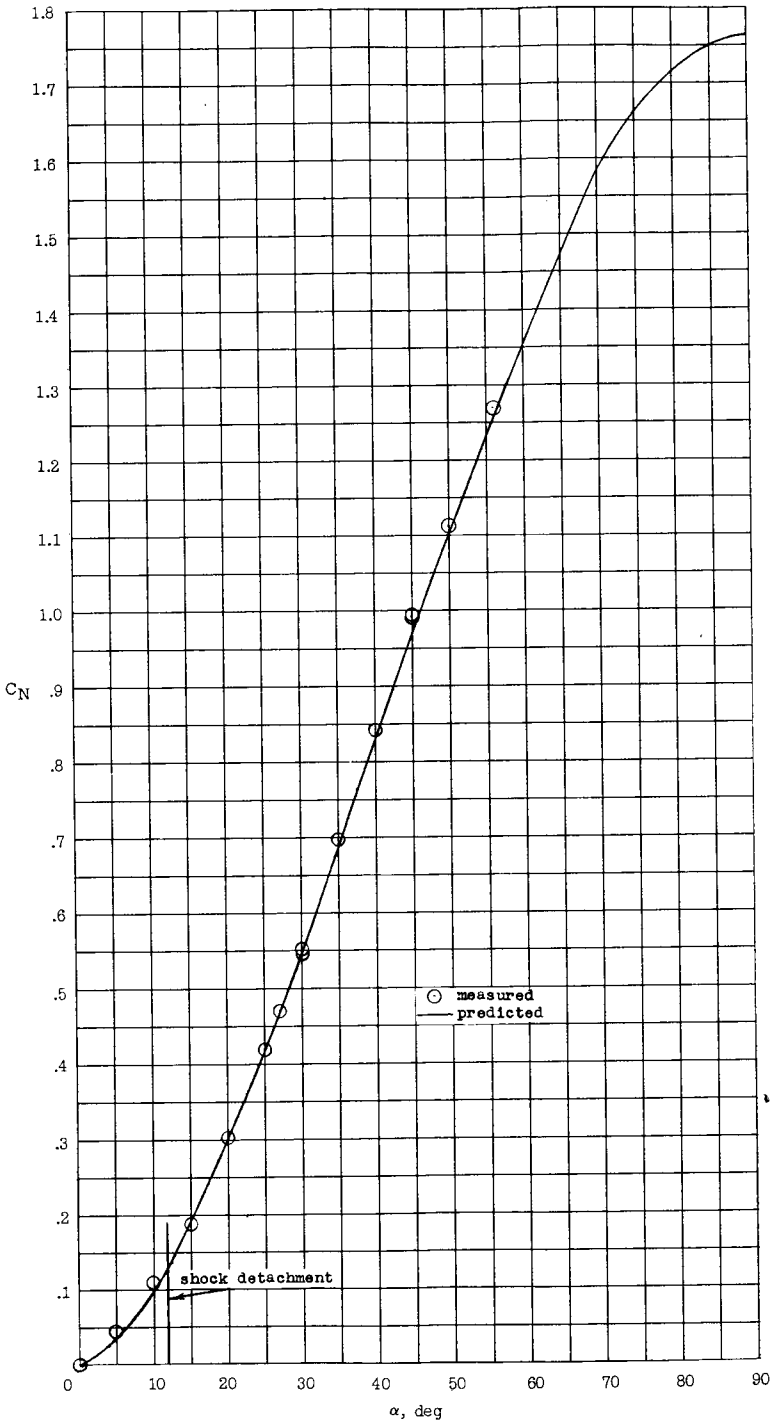


Figure 20.- Variation of normal-force coefficient with angle of attack for present undeflected wing.